International Journal of Heat and Mass Transfer 194 (2022) 123016

Contents lists available at ScienceDirect

International Journal of Heat and Mass Transfer

journal homepage: www.elsevier.com/locate/hmt

Machine learning enabled condensation heat transfer measurement

Siavash Khodakarami[a], Kazi Fazle Rabbi[a], Youngjoon Suh[c], Yoonjin Won[c,d], Nenad Miljkovic[a,b,e,f,*]

[a] Department of Mechanical Science and Engineering, University of Illinois at Urbana – Champaign, Urbana, IL 61801 United States
[b] Department of Electrical and Computer Engineering, University of Illinois at Urbana – Champaign, Urbana, IL 61810 United States
[c] Department of Mechanical and Aerospace Engineering, University of California, Irvine, Irvine, CA 92697 United States
[d] Department of Electrical Engineering and Computer Science, University of California, Irvine, Irvine, CA 92697 United States
[e] Material Research Laboratory, University of Illinois at Urbana – Champaign, Urbana, IL 61801 United States
[f] International Institute for Carbon Neutral Energy Research (WPI-I2CNER), Kyushu University, 744 Motooka, Nishi-ku, Fukuoka 819-0395, Japan

ARTICLE INFO

Article history:
Received 9 February 2022
Revised 26 April 2022
Accepted 8 May 2022
Available online 27 May 2022

Keywords:
Condensation
Heat transfer
Machine learning
Machine vision
Droplet

ABSTRACT

Measuring condensation heat transfer and its associated heat transfer coefficient is not trivial. Rigorous measurements require careful experimental design and tradeoff studies to properly select sensor type, sample geometry and size, coolant fluid and flow rate, operating conditions, working fluid purity, purge methodology, and measurement protocol. Conventional tube-based condensation heat transfer measurements quantify the change in the enthalpy of a single-phase coolant flow via measurement of the inlet and outlet bulk coolant temperatures. The uncertainties associated with this classical and well-established experimental method are high. The high uncertainty stems from the high characteristic heat transfer coefficient or heat flux associated with the condensation process, making the thermal resistance on the external tube side typically on the same order of magnitude as the internal single-phase coolant convective heat transfer thermal resistance. Even when taking the utmost care and using extremely accurate sensors having low uncertainty, the relative uncertainties of heat flux and heat transfer coefficient can be in the range of 20% to 100%. Here, we take advantage of machine learning (ML) to develop an optical visualization method for dropwise condensation heat transfer characterization. Using state-of-the-art intelligent vision, we demonstrate a previously-unexplored method for characterizing the condensate droplet shedding frequency, droplet shedding size, and heat flux without the need for high-speed imaging. We verify our technique by conducting rigorous steam condensation measurements on Parylene C coated smooth copper tube samples having 500 nm, 1 μm, and 5 μm Parylene C thicknesses. We validate our ML predictions with data obtained simultaneously using the enthalpy-change method on a custom and well-established condensation chamber. In contrast to conventional heat transfer measurement methods, the uncertainty of our ML method is constant (~10%) and does not vary with heat flux. We finally demonstrate the key advantage of our ML measurement technique on a custom-made tube having axially varying surface properties resulting in differing local heat transfer coefficient. Our ML heat transfer measurement method enables the high fidelity characterization of phase change heat flux, reduction in relative measurement uncertainty, resolution of local effects, and elimination of the need for temperature measurement across samples.

1. Introduction

Condensation is an important phase-change phenomenon to a plethora of industries. In particular, dropwise condensation (DWC) has been the topic of great interest in the past century due to its potential to enhance the thermal efficiency of applications such as high heat flux electronics thermal management [1], the steam power cycle used for power generation [2], and building heating and cooling [3]. The key to efficient DWC is the rapid removal of condensate droplets from the condensing surface. Efficient droplet removal minimizes the conduction thermal resistance of the condensate liquid remaining on the surface. DWC mainly occurs on nonwetting surfaces where contact angle hysteresis is typically low [4]. This droplet removal relies on gravity or vapor shear and typically happens when the droplet size approaches the capillary length (~2.7 mm for water) of the condensate [5].

* Corresponding author at: University of Illinois at Urbana-Champaign 2136 Mechanical Engineering Laborat, 105 South Mathews Avenue, Urbana, IL 61801, United States.
E-mail address: nmiljkov@illinois.edu (N. Miljkovic).

https://doi.org/10.1016/j.ijheatmasstransfer.2022.123016
0017-9310/

Nomenclature

Symbols

A	Surface area
Al	Aluminum
ANN	Artificial neural network
BiFPN	Bi-directional feature pyramid network
c	Specific heat
Cu	Copper
d	Used to refer to parameters uncertainty
D	Diameter
DAQ	Data acquisition system
DCNN	Deep convolutional neural network
DI	Deionized
DWC	Dropwise condensation
EES	Engineering Equation Solver
ESEM	Environmental scanning electron microscopy
Exp	Experimental
f	Friction factor
F	Droplet shedding frequency
fps	Frame per second
FWC	Filmwise condensation
g	Acceleration due to gravity
h	Heat transfer coefficient
H	Image height
HCl	Hydrochloric acid
I	Image (pixel) intensity
IoU	Intersection over union
k	Thermal conductivity
L	Length
LMTD	Log mean temperature difference
$\dot{m}$	Mass flow rate
ML	Machine learning
MSE	Mean square error
NCG	Non-condensable gas
P	Pressure
Pr	Prandtl number
q''	Heat flux
Re	Reynolds number
Ref	Refrigerant
RGB	Red-Green-Blue color space
RNN	Recurrent neural network
RTD	Resistance thermal detector
SSIM	Structural similarity index metric
T	Temperature
U	Overall heat transfer coefficient
V	Droplet volume
$\dot{V}$	Volumetric flow rate
W	Image width

Greek symbols

Δ	Difference
μ	Dynamic viscosity
λ	Mean image intensity
σ	Standard deviation
ρ	Density
θ	Droplet contact angle

Subscripts

a	Advancing (droplet contact angle)
b	At bulk
c	Coolant
con	Condensation
fg	Associated with latent heat of vaporization
in	Inlet
o	Outer or outside
out	Outlet
r	Receding (droplet contact angle)
s	At surface
sat	Saturated state
tube	tube

For both filmwise condensation on bare surfaces or DWC on promoted surfaces, the experimental characterization of condensation heat transfer requires particular attention to be paid to sensor selection and measurement protocols. Condensation experiments are usually conducted in vacuum-compatible chambers to limit the presence of non-condensable gases (NCGs) that greatly degrade the heat transfer measurement. Even trace amounts of NCGs, as low as a few PPM, can degrade the measured heat transfer coefficient by as much as 50% [6,7]. When testing condenser tube surfaces, heat flux is calculated by measuring the coolant bulk inlet and bulk outlet temperatures inside of the tube. Knowledge of the coolant inlet and outlet temperatures as well as the saturated vapor temperatures enables the use of the log mean temperature difference [8] to determine the overall vapor-to-coolant heat transfer coefficient (U). This overall quantity can then be used with the internal heat transfer coefficient (h_i) on the coolant side to estimate the external condensation heat transfer coefficient (h_{con}).

The typical uncertainties associated with condensation heat flux (q") and heat transfer coefficient estimations are relatively high. Small errors in temperature measurements propagate into high uncertainties in the estimations. Many past studies have measured the condensation heat transfer on flat surfaces by carefully inserting several temperature sensors at specified locations inside a copper block on which the sample is mounted. Assuming one-dimensional steady-state heat conduction, and knowing the distance between the thermocouples, the heat flux can be calculated. A separate temperature sensor is required at a location close to the surface of the sample and inside the copper block in order to estimate the condensing surface temperature and to calculate h_{con} [9,10]. The temperature differences measured are quite small ($\Delta T = 1 - 3$ K) and may lie within the uncertainty of the temperature sensors used [11]. Furthermore, carful installation of the sensors to ensure good thermal contact and orthogonality to the surface normal is challenging. To ameliorate these difficulties, researchers have also attempted to quantify the condensation heat transfer on tube geometries. Similar challenges exist on tubes where sensors need to be placed at the centerline of the tube to measure the bulk fluid temperature. Furthermore, highly turbulent coolant flow having high Reynolds number ($Re_d > 20{,}000$) is required to minimize the radial temperature gradient in the coolant flow at the inlet and outlet.

Recently, an innovative approach called the thermal amplification technique [12] was created to reduce condensation heat transfer measurement uncertainty. The approach uses a high coolant flow rate in the primary test section to ensure that the governing thermal resistance is on the condensation side as opposed to the coolant side. Then, the method uses a heat exchanger to couple the primary loop to a secondary loop having a cooling water stream with a much lower flow rate in order to measure higher temperature differences and achieve higher signal-to-noise ratio. The measured temperature difference in the secondary loop was two orders of magnitude larger than the primary loop due to the reduction in flow rate. Although thermal amplification was able to achieve uncertainties of 10%, it is complex.

A significant source of error of coolant enthalpy-change-based condensation heat transfer measurement techniques, including the thermal amplification technique, is the importance of spatial location of the temperature sensor inserted inside the coolant flow. This particular sensitivity to probe location stems from the fact that the coolant temperature profile is not uniform for developing or fully-developed internal pipe flows [13]. As such, it is very important to install both the inlet and outlet sensor at the same radial location inside the tube in reference to the tube inner wall location. Moreover, cases exist where measuring the bulk fluid temperature is not feasible. For example, when the flow is laminar and a flow mixer is not present [14].

A lack of accurate correlations for internal heat transfer coefficient for more complex geometries and conditions (e.g., internally enhanced tubing, thermally and hydrodynamically developing flow) is yet another limitation of conventional methods. Therefore, a need exists to develop a more robust, raid, and simple approach to measure the condensation heat transfer which can be applicable at different flow conditions, for different tube geometries, and that is insensitive to temperature sensor accuracy or position.

A common alternative method to the coolant enthalpy-change approach eliminates the use of temperature sensors and uses collected condensate mass or volume falling from the condensing surface to estimate the condensation heat transfer rate [15,16]. However, the precise collection of condensates from the condensing surface of interest over time is challenging as condensation can occur on tertiary surfaces such as chamber walls, fittings, and connections, resulting in accumulation error. To alleviate these errors, the condensate collector needs to be installed inside the condensation chamber and at the proper position relative to the condensing surface, adding additional complexity and a source of uncertainty. Moreover, the collector should possess real-time measurement capability as the condensation rate varies with vapor pressure and takes time to reach to steady-state. These challenges result in relatively high uncertainty in the measurements and therefore the enthalpy change-based method has been the preferred method of choice in the past decade when compared to the mass collection method.

In the past decade, many studies have focused on developing surfaces to increase droplet-shedding frequency and decrease the droplet shedding size during DWC. These surfaces can be classified as hydrophobic [17], superhydrophobic [18], hybrid or biphilic [19,20], liquid infused [21], and slippery hydrophilic [4]. Despite the progress in surface design and DWC heat transfer enhancement, much less attention has been given to improving characterization methods for reducing the condensation heat transfer measurement uncertainty. Although reporting uncertainty values is pivotal to understand, compare, and contrast surface heat transfer performance, many studies report only the heat flux and heat transfer coefficient values without conducting error propagation analysis to evaluate the uncertainty of their results [11]. Among the studies which have reported the uncertainty values for their heat transfer measurements, uncertainties range from 12% to 60% for heat flux and 20% to 80% for condensation heat transfer coefficient [5,22–26].

In an effort to simplify and speed up heat transfer quantification, several studies have developed visualization techniques to gain understating of DWC droplet dynamics. Environmental scanning electron microscopy (ESEM) represents an appropriate approach for investigating micro/nanoscale droplet growth dynamics during DWC [27,28]. Although ESEM represents a powerful observation tool, it is expensive and cannot be used for the heat flux and heat transfer coefficient measurement mainly due to time resolution challenges.

A second visualization method used to study droplet dynamics during DWC is high-speed optical imaging. By recording videos of DWC at a very high frame rate ($>$ 200 frame per second (fps)) using a high-speed camera, the heat transfer characteristics can be studied. This was done in the past using high-speed images to capture 10 s duration DWC videos at 200 fps. These images were then converted to black and white to facilitate the detection of falling droplets in order to estimate the falling droplet frequency on tubes having hybrid wettability [29]. Drawbacks exist when using high frame rate videos for heat flux estimation. First, a high-speed camera is required, which is expensive. Second, recording high speed videos at high frame rates results in large data file sizes. Therefore, the real-time video duration is limited to only tens of seconds ($\sim$10 s). As a result, the frequency of shedding droplets is calculated by averaging over a short time period which results in poor time-averaged accuracy. Therefore, it would be beneficial to have high-fidelity heat flux estimation using shedding droplet detection at relatively low frame rates ($<$ 60 fps). This remains a challenge as falling droplets from condensing tubes move too quickly to be resolved accurately at low frame rates, resulting in deformed or blurry images.

A promising pathway to overcome this imaging challenge is to use recently developed learning-based computer vision techniques to detect and resolve deformed droplets. Remarkable progress has been made in computer vision techniques using deep convolutional neural networks (DCNNs) for classification [30], object detection [31], semantic and instance segmentation [32]. DCNNs do not require hand-crafted feature selection. Instead, a hierarchy of features at different scales is extracted by using several convolutional layers that are activated by non-linear functions such as sigmoid, ReLU, and Leaky ReLU and are connected to each other through pooling layers [33]. Therefore, DCNNs are invariant to translation and objects can be detected at spatially varying locations. Also, a well-trained DCNN can be illumination-invariant [34] and therefore desirable for characterization of condensation experiments that are done at different lighting conditions and with differing optical properties of the condensing surface.

Recently, multiple thermofluidic studies have investigated the combination of visual data along with deep neural network models for two-phase heat transfer prediction. One study custom designed a CNN with two convolutional layers followed by a fully connected layer to enable nucleate pool boiling heat flux estimation [35]. The study reported a mean average percentage error as low as 10% over the validation and test datasets for nucleate boiling heat flux. Although demonstrating promising results, the model developed was system-dependent and not universal. Follow on work developed a hybrid physics-informed framework for boiling heat flux prediction using visual data [36]. The model consisted of a combination of the VGG16 DCNN [37] and Mask R-CNN [32] algorithms for feature extraction. The outputs of these two networks were additionally processed through a fully connected layer for heat flux prediction. Using the hybrid framework, they reported a pool boiling curve prediction with a mean error of 6%.

Although promising, intelligent-vision techniques for external condensation have been less explored. Potential exists to use these state-of-the-art techniques for condensation characterization, especially during DWC and jumping droplet condensation [38]. In this work, we first conduct a rigorous uncertainty analysis for conventional methods for external condensation characterization, demonstrating the necessity of using more reliable measurement methods to attain higher certainty levels as well as simplified characterization. We then propose a simple, yet powerful, learning-based algorithm that requires low frame rate ($\sim$ 30 fps) video imaging as the input to the falling droplet detection network. The output of the network is then processed for robust and accurate condensation heat flux measurement. We verified our method by conducting rigorous steam condensation measurements on a Parylene C coated copper tube samples having 500 nm, 1 μm, and 5 μm thick-

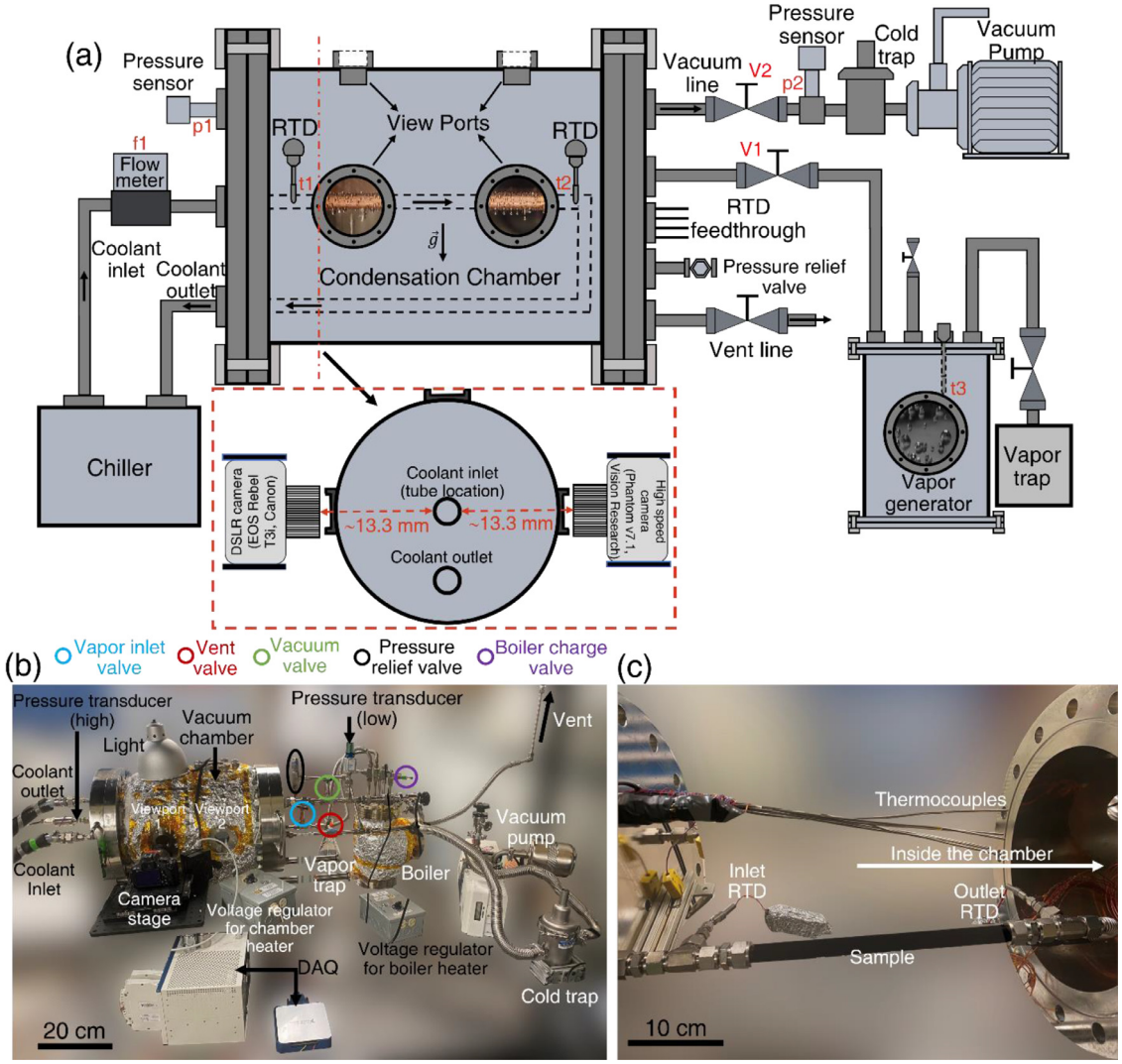

Fig. 1. (a) Schematic and (b) photograph of the test facility used for condensation heat transfer measurement and visualization. Schematic not to scale. Inset of (a): cross sectional view at the dash-dot line in (a) depicting the optical access of the sample. (c) Photograph of the chamber when opened showing the tube sample with internal components. A summary of instrumentation with span and corresponding uncertainty are shown in Table 1.

nesses in a custom condensation chamber. We validated the data using the classical coolant enthalpy-change method using water as the coolant fluid. In contrast to the conventional method where the uncertainty varied with tube geometry, flow condition, sensors uncertainty, and condensation heat flux, our method achieved a constant relative uncertainty of ~10% for all cases tested. Using only optical visualization data, we show that our technique is also capable of achieving local heat transfer measurement. To demonstrate the utility of our technique for local axially varying heat fluxes on a tube sample, we fabricated a single tube with axially varying wetting properties, leading to different condensation heat transfer modes for each section on a single sample. Using our approach, we measured the local heat fluxes on the three different surfaces having differing wetting properties using a single experiment.

2. Experimental setup

To obtain visualization data, and to conduct classical coolant enthalpy-change heat transfer measurements, experiments were conducted in the test facility shown in Fig. 1. The facility was built as part of past condensation heat transfer experiments, the details of which can be found here [39,40]. Briefly, the facility consists of a custom developed stainless steel vacuum/pressure chamber (Gladwin Tank) in which condensation occurs (shell) on an internal sample (tube). The system also consists of a steam supply system (Kurt J. Lesker) and an independent coolant flow loop. The internal diameter of the chamber (shell) is 30.5 cm and the maximum straight tube length tested inside the chamber can be as long as 30 cm. Each end of the chamber is sealed with 44.5 mm thick stainless steel flanges. Both flanges have several feedthrough fittings allowing thermocouple, resistance temperature detector (RTDs), fluidic, and pressure transducer installation. Two independent pressure transducers (MicroPirani, MKS Instruments and Baratron 728A) were installed on the chamber to monitor the pressure inside when vacuuming the chamber and throughout DWC experiments. Finally, 6 optical viewports (5.08 cm diameter ports from MPF Products and 6.35 dimeter ports from MDC Vacuum) were installed on the chamber for ease of visualization. The viewports are designed for internal pressures up to 2.75 MPa and can operate in vacuum conditions. Next to the chamber, the steam supply system (Standard CF TEE, Kurt J. Lesker with 20.3 cm outer diameter) is filled with deionized (DI) water which is heated by tape heaters (Part #AWH-101-040DP, ETS Equipment) that are installed on the outer surface of the vapor generator. The heating rate of the tape heaters is controlled by connecting the tape heaters to a variable voltage regulator (Model PM-1220B, ETS Equipment). The DI wa-

ter temperature was monitored during the heating process by a T-type thermocouple (Part #SCPSS-032, Omega) which was passed into the vapor generator. The vapor generator had four ports on top that were manufactured into a custom made CF blank by Kurt J. Lesker. These ports were used to connect the vapor generator to the line connecting to the main chamber, a pressure relief valve set at 300 kPa (Part #SS-RL4S8, Swagelok), a vapor vent line to avoid over-pressurization, and a fill line used to fill the vapor generator with DI water.

At the coolant flow loop, water is cooled using a large capacity chiller (Part #327005091602, System III TU7 Pump, Thermo Fisher Scientific) and routed to the test section inside the chamber. The coolant flow rate was measured using an electromagnetic flow meter (Part #FMG93, Omega). The coolant inlet and outlet temperatures were measured using two RTDs (Part #AT-PX1123Y-LR4S1T2T, ReoTemp) located at the entrance and exit of the test tube sample. All auxiliary connections and tubing inside the chamber were insulated to prevent condensate formation and to limit condensation to occur on the test tube only. Also, the chamber itself was wrapped with tape heaters (Part #AWH-101-040DP, ETS Equipment) that were controlled with a voltage regulator (Model PM-1220BE, ETS Equipment) to gently heat the chamber and prevent condensate formation on the internal side of the chamber wall and viewports. The pressure of the condensing vapor was controlled by throttling a manual valve (Model #6L-LD8-BBXX, Swagelok) connecting the vapor generator to the chamber (labeled V1 in Fig. 1).

Non-condensable gases were removed from the system by using a vacuum pump (Model Alcatel 2005) that was turned on prior to each experiment. A liquid nitrogen cold trap (Model #TLR4 × 1100QF, Kurt J. Lesker) was installed in line between the chamber and the vacuum pump to remove any moisture from the air, which improves the quality of the vacuum and protects the pump. While pumping down the chamber, the heaters around the vapor generator were also turned on to boil the DI water. However, the valve (Model #6L-LD8-BBXX, Swagelok) connecting the vapor generator the chamber was kept closed at this stage. After the chamber pressure reached 200 Pa, the coolant line was initiated to work so that the coolant inlet and outlet temperature would reach to the steady values before the measurement started.

After the chamber pressure reached below 2 Pa, the DI water was allowed to boil for at least 10 min, and the coolant inlet and outlet reached steady state, the condensation experiment was started. At this point, the valve (Model #6L-LD8-BBXX, Swagelok) connecting the vacuum pump to the chamber (labeled V2 in Fig. 1) was closed and the vapor was let into the chamber with pressure set by adjusting the valve position on the valve between the vapor generator and the chamber (labeled V1 in Fig. 1). For every measurement made at a certain vapor pressure, we made sure to reach steady state (± 50 Pa pressure oscillation) and report steady state values. All measurements were collected through a special high-accuracy data acquisition system (DAQ, PXIe 1073, National Instruments) and analyzed with LabVIEW. The PXIe DAQ was specifically chosen to provide the highest possible fidelity in enthalpy measurements with minimal DAQ uncertainty. A summary of instrumentation with span and corresponding uncertainty are shown in Table 1.

3. Uncertainty analysis

In conventional heat transfer experiments, the heat flux on the outside of the tube is measured by calculating the enthalpy change of the coolant flowing inside of the tube, as described in Eq. (1), where $c_{p,c}$ is the coolant specific heat capacity, $\dot{m}_c$ is the coolant mass flow rate, $T_{c,out}$ is the coolant outlet temperature, $T_{c,in}$ is the coolant inlet temperature, and A_o is the external surface area of the tube. The outer area of the smooth tube is calculated with Eq. (2), where D_o and L are the outer diameter and length of the tube, respectively. Using the log mean temperature difference (ΔT_{LMTD}) method, the overall heat transfer coefficient (U) of the tube can be computed by Eq. (3), where ΔT_{LMTD} is calculated using Eq. (4). Here, T_{sat} is the saturated vapor temperature. The calculated U contains the convective resistances on the inner and outer walls of the tube as well as the heat conduction resistance through the tube wall and any applied coating layer to promote DWC. The coolant-side convective heat transfer coefficient (h_{in}) is usually calculated using the Petukhov correlation [41] for turbulent flow using Eqs. (5) and (6), where Re represents the internal flow Reynolds number based on the internal tube diameter (D_i) and is defined by Eq. (7), Pr is the coolant Prandtl number, f is the pipe friction factor, k is the coolant thermal conductivity, μ_b and μ_s are the dynamic viscosities of the coolant at the bulk fluid temperature and at the tube wall temperature, respectively, and $n = 0.11$ when the fluid is heated and $n = 0.25$ when the fluid is cooled [42]. Knowing h_{in}, we can divide the U into three different thermal resistance components of internal convection, tube wall heat conduction, and external condensation as shown in Eq. (8), where h_{con} is the condensation heat transfer coefficient, k_{tube} is the thermal conductivity of the tube material, and A_i is the internal surface area of the tube. Therefore, a closed form solution can be obtained for h_{con} which is shown in Eq. (9).

$$q'' = \frac{c_{p,c}\dot{m}_c(T_{c,out} - T_{c,in})}{A_o} \quad . \tag{1}$$

$$A_o = \pi D_o L \quad . \tag{2}$$

$$U = \frac{q''}{\Delta T_{LMTD}} \quad . \tag{3}$$

$$\Delta T_{LMTD} = \frac{(T_{sat} - T_{c,in}) - (T_{sat} - T_{c,out})}{\ln\left[\frac{(T_{sat} - T_{c,in})}{(T_{sat} - T_{c,out})}\right]} \quad . \tag{4}$$

$$h_{in} = \left(\frac{k}{D_i}\right)\frac{\left(\frac{f}{8}\right)\mathrm{RePr}}{1.07 + 12.7\left(\frac{f}{8}\right)^{\frac{1}{2}}\left(\mathrm{Pr}^{\frac{2}{3}} - 1\right)}\left(\frac{\mu_b}{\mu_s}\right)^n \quad . \tag{5}$$

$$f = [0.79\ln(\mathrm{Re}) - 1.64]^{-2} \quad . \tag{6}$$

$$\mathrm{Re} = \frac{4\rho\dot{V}}{\pi\mu D_i} \tag{7}$$

Table 1
Details of test facility instrumentation and uncertainty of each sensor. Numbering in the measurement column corresponds to the locations identified in Fig. 1(a).

Measurement	Instrument	Loc.	Span	Uncertainty
Coolant temperatures	Class AA RTD	t1, t2	7-20 °C	0.15 °C ± 0.12%
Vapor temperature	T-type thermocouple	t3	20-100 °C	± 0.5 °C
Coolant flow rate	Electromagnetic flow meter	f1	11-30 L/min	± 1%
Chamber pressure	Pressure transducer (Pirani)	p2	0-17 kPa	± 1%
Chamber pressure	Pressure transducer (Baratron)	p1	0.133-133 kPa	0.5 - 1%
Tube length	Caliper		0-30 cm	± 0.5 mm
Tube diameter	Provided by vendor		-	± 0.1 mm

$$\frac{1}{UA} = \frac{1}{h_{con}A_o} + \frac{\ln\left(\frac{D_o}{D_i}\right)}{2\pi L k_{tube}} + \frac{1}{h_{in}A_i} \ . \tag{8}$$

$$h_{con} = \left(\frac{1}{U} - \frac{A_o}{h_{in}A_i} - \frac{A_o \ln\left(\frac{D_o}{D_i}\right)}{2\pi L k_{tube}}\right)^{-1} \ . \tag{9}$$

The uncertainty of the measured heat flux is dependent to the uncertainties of the inlet and outlet temperatures, mass flow rate, diameter and length of the tube measurements. The relative uncertainty of the heat flux can be calculated by Eq. (10). Uncertainty of the temperature difference is defined in Eq. (11), where dT is the coolant inlet and outlet temperature measurement error:

$$\frac{dq''}{q''} = \sqrt{\left(\frac{d\dot{m}_c}{\dot{m}_c}\right)^2 + \left(\frac{d(T_{c,out} - T_{c,in})}{(T_{c,out} - T_{c,in})}\right)^2 + \left(\frac{dD_o}{D_o}\right)^2 + \left(\frac{dL}{L}\right)^2} \tag{10}$$

$$d(T_{c,out} - T_{c,in}) = \sqrt{2}dT \tag{11}$$

Analyzing Eq. (10), we see that the heat flux relative uncertainty is very sensitive to the accuracy of the mass flow rate, and inlet/outlet temperatures measurements. Furthermore, at a fixed mass flow rate and fixed inlet temperature, the outlet temperature increases with increasing heat flux and the ratio of the outlet temperature measurement error to the measured temperature value reduces, resulting in a smaller relative uncertainty for the heat flux measurement.

Longer tubes with higher diameters are also preferred in order to increase the temperature difference across the tube leading to higher signal-to-noise ratio. A similar uncertainty analysis could be conducted for measured h_{con}. The uncertainty analysis on U which is necessary for conducting the uncertainty analysis of h_{con} is shown in Eq. (12), where $d\Delta T_{LMTD}$ is shown in Eqs. (13) to (16). The error of the saturation temperature (dT_{sat}) could be defined by the error of the thermocouple installed inside the chamber or the pressure sensor measuring the chamber saturation pressure. Here, to simplify Eq. (13), we assume that this error is comparable to the dT ($dT_{sat} \approx dT$). Therefore, a simplified version of Eq. (13) is shown in Eq. (16).

$$\frac{dU}{U} = \sqrt{\left(\frac{d\dot{m}_c}{\dot{m}_c}\right)^2 + \left(\frac{d(T_{c,out} - T_{c,in})}{(T_{c,out} - T_{c,in})}\right)^2 + \left(\frac{dD_o}{D_o}\right)^2 + \left(\frac{dL}{L}\right)^2 + \left(\frac{d\Delta T_{LMTD}}{\Delta T_{LMTD}}\right)^2} \tag{12}$$

$$\frac{d\Delta T_{LMTD}}{\Delta T_{LMTD}} = \frac{\sqrt{(dT_{sat})^2(T_{c,out} - T_{c,in})^4 + (dT)^2(T_{sat} - T_{c,out})^2 A + (dT)^2(T_{sat} - T_{c,in})^2 B}}{(T_{sat} - T_{c,out})(T_{sat} - T_{c,in})\left(\ln\left[\frac{(T_{sat} - T_{c,in})}{(T_{sat} - T_{c,out})}\right]\right)^2} \tag{13}$$

$$A = \left(T_{c,in} - T_{c,out} + (T_{sat} - T_{c,in}) \ln\left[\frac{(T_{sat} - T_{c,in})}{(T_{sat} - T_{c,out})}\right]\right)^2 \tag{14}$$

$$B = \left(T_{c,in} - T_{c,out} + (T_{sat} - T_{c,out}) \ln\left[\frac{(T_{sat} - T_{c,in})}{(T_{sat} - T_{c,out})}\right]\right)^2 \tag{15}$$

$$\frac{d\Delta T_{LMTD}}{\Delta T_{LMTD}} = dT \frac{\sqrt{(T_{c,out} - T_{c,in})^4 + (T_{sat} - T_{c,out})^2 A + (T_{sat} - T_{c,in})^2 B}}{(T_{sat} - T_{c,out})(T_{sat} - T_{c,in})\left(\ln\left[\frac{(T_{sat} - T_{c,in})}{(T_{sat} - T_{c,out})}\right]\right)^2} \tag{16}$$

Conducting the uncertainty analysis for U, the uncertainty analysis of h_{con} is done using Eq. (9) and is shown in Eq. (17), where B_{1-4} are defined by Eqs. (18) to (21). The relative uncertainty of the internal convective heat transfer coefficient (dh_{in}/h_{in}) is dependent to the accuracy of the correlation used for estimating the internal heat transfer coefficient (h_{in}). In case of the Petukhov correlation (Eq. 5), the uncertainty of h_{in} is reported to be 6% [24,41].

$$dh_{con} = \frac{2\sqrt{B_1 + B_2 + B_3 + B_4}}{\left(UD_oD_i \ln\left(\frac{D_o}{D_i}\right) + 2UD_ok - 2D_ih_{in}k\right)^2} \ . \tag{17}$$

$$B_1 = 4U^4 D_o^2 D_i^2 k^4 (dh_{in})^2 \ . \tag{18}$$

$$B_2 = U^4 D_i^2 k^2 h_{in}^2 (dD_o)^2 \left(D_i h_{in}\left(\ln\left(\frac{D_o}{D_i}\right) + 1\right) + 2k\right)^2 \ . \tag{19}$$

$$B_3 = U^2 k^2 h_{in}^2 (dD_i)^2 (UD_oD_ih_{in} + 2UD_ok)^2 \ . \tag{20}$$

$$B_4 = 4D_i^4 h_{in}^4 k^4 (dU)^2 \ . \tag{21}$$

It is important to note, the aforementioned analysis is predicated on ensuring that the internal coolant flow is highly turbulent ($Re > 10{,}000$) and the flow is hydrodynamically fully developed, both of which are necessary conditions to ensure high accuracy for the Petukhov correlation (Eq. 5). Turbulence in particular is of upmost importance as any laminar flow results in significant radial temperature profile development within the internal coolant flow, making the measurement of bulk fluid temperature difficult unless highly efficient flow mixers are installed. To achieve reasonable results, $Re > 10{,}000$ is necessary.

Fig. 2 shows the uncertainty analysis results for the condensation heat flux as a function of tube length (L) and outer diameter (D_o), heat flux (q"), and the absolute uncertainty of the temperature sensor (dT). Fig. 2(a) and 2(b) show the relative heat flux uncertainty (dq'') when the uncertainty of the temperature measurement sensor is $dT = 0.1$ °C, corresponding to the uncertainty of the class AA RTDs used in the experimental results of this work (Table 1). Fig. 2(c) and (d) show dq'' when the uncertainty of the temperature sensor is $dT = 0.5$ °C, corresponding to an approximated case where a calibrated thermocouple is used, which comprises of a combination of the uncertainty due to data fitting (standard deviation) combined with the uncertainty of the instrument (typically an RTD) used for calibration. We note that the uncertainty of the thermocouples can vary based on the thermocouple type and quality of the manufacturing and can be as high as ±2 °C. Here, we chose a value which is at the low range of common thermocouple uncertainties [43]. The results show that the dq'' is very sensitive to the accuracy of the temperature sensors. For example,

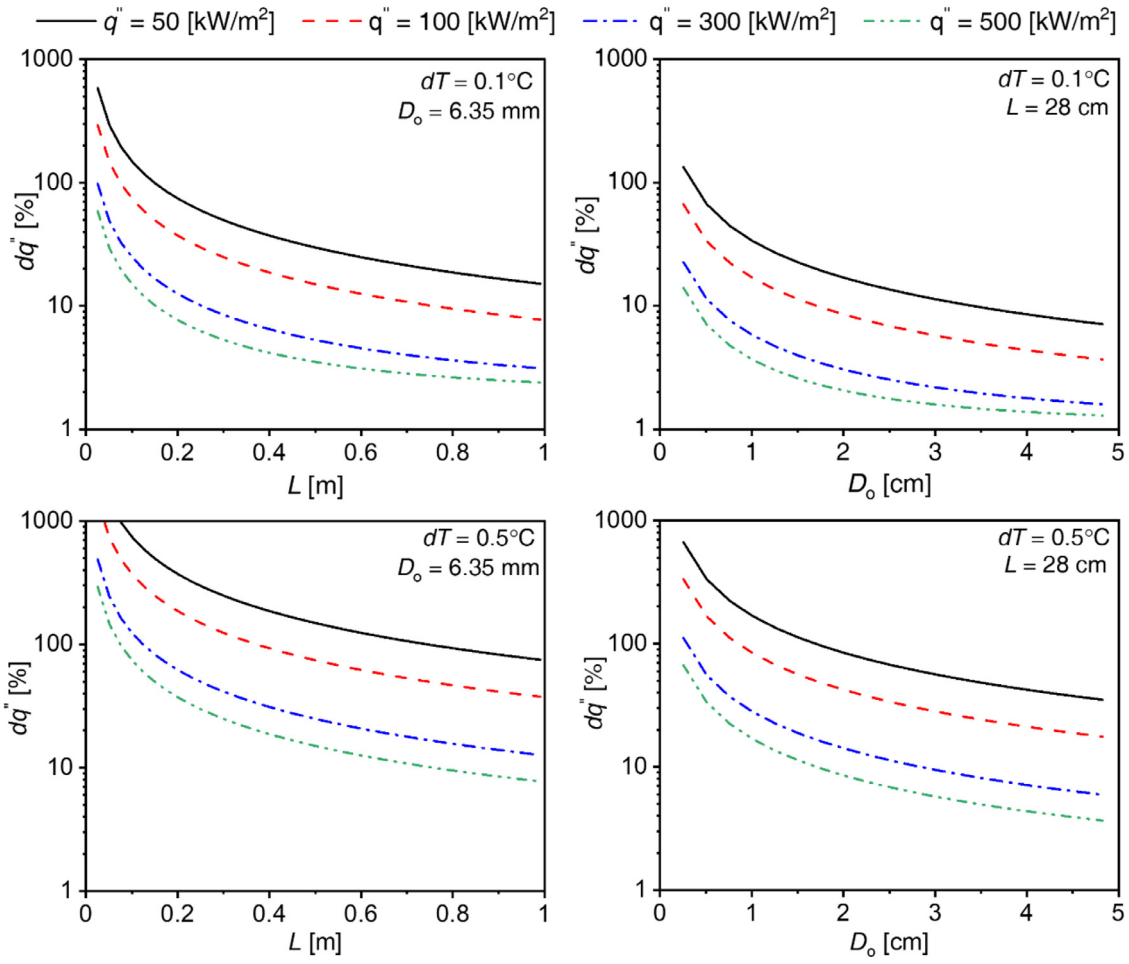

Fig. 2. Uncertainty analysis results for external tube condensation heat flux. (a) Condensation heat flux relative uncertainty (dq'') as a function of tube length (L) and heat flux (q") for a fixed tube outer diameter of $D_o = 6.35$ mm (1/4" DIA tubing) and temperature sensor uncertainty $dT = 0.1$ °C. (b) dq'' as a function D_o and q" for fixed $L = 28$ cm and $dT = 0.1$ °C. (c) and (d) show the same dq'' analysis presented in (a) and (b) but for $dT = 0.5$ °C temperature uncertainty. For this analysis, the coolant was tap water, and the coolant flow rate was 15 LPM for all cases. This corresponds to Re = 48833 for $D_i = 4.7$ mm. The legends on top of the figures are valid for all graphs. Tube wall thickness is 1.6 mm for all cases.

the heat flux uncertainty is 3 to 4 times higher when dT increases from 0.1 °C to 0.5 °C for a fixed tube length and tube diameter.

It is important to note that our analysis is conservative in that it completely ignores the uncertainty component from the data collection process and the DAQ system itself. In fact, DAQ uncertainty must be accounted for any measurement, with DAQ uncertainty components for temperature measurements using high quality DAQ cards (NI 9217 4-Ch PT100 RTD 24-bit card or a NI 9213 Spring, 16-ch TC, 24-bit card) approaching ±1 °C. Even the PXIe DAQ used in our experimental setup has a DAQ uncertainty of ±0.1 °C for associated RTD measurements.

Common tubes lengths used for testing condensation performance of promoter coatings and nanoengineered surfaces are typically less than $L = 50$ cm with diameters $D_o < 1.3$ cm [40,44–47]. Therefore, heat flux uncertainties up to $dq'' \approx 100\%$ are unavoidable for conventional experimental measurement methods.

The relative uncertainty analysis of the condensation heat transfer coefficient (dh_{con}) for a variety of tube sizes (L and D_o) and h_{con} as a function of coolant volumetric flow rate ($\dot{V}$) is shown in Fig. 3. The dh_{con} generally decreases with increasing coolant flow rate because higher flow rates result in higher h_{in}. The higher h_{in} reduces the internal convective thermal resistance, enhancing the relative contribution of the external condensation heat transfer resistance to the overall steam-to-coolant thermal resistance. However, for some cases (e.g., low h_{con}) where the heat transfer is mainly limited by the external condensation side, increasing the flow rate negatively affects the relative error because the absolute error for h_{in} increases with marginal effect on the temperature difference across the tube due to the limits from the external condition. Higher coolant flow rates (higher Re) are required for higher values of h_{con} in order to maintain a reasonable thermal resistance ratio with the external condensation heat transfer thermal resistance.

Fig. 3(a) shows the uncertainty analysis of the dh_{con} where uncertainty levels are higher for higher h_{con} values at low coolant flow rates. This trend occurs because heat transport is mainly limited by the internal coolant thermal resistance rather than the condensation itself. However, uncertainty decrease faster with increasing coolant flow rate for higher h_{con} values. This indicates the importance of lowering the internal heat transfer resistance via utilizing higher coolant flow rates, enhanced (finned) internal surfaces [48,49], or flow perturbation or modification [50], in order to attain reliable external condensation heat transfer measurements.

Fig. 3(b) shows the effect of tube length (L) and coolant flow rate on dh_{con}. As expected, longer tube length is preferable to increase the coolant inlet-to-outlet temperature difference and signal-to-noise ratio. Analysis of the tube diameter on dh_{con} (Fig. 3c) reveals a similar result as that observed in Fig. 3(a), where higher coolant flow rates are required for larger diameter tubes to achieve the same internal flow thermal resistance.

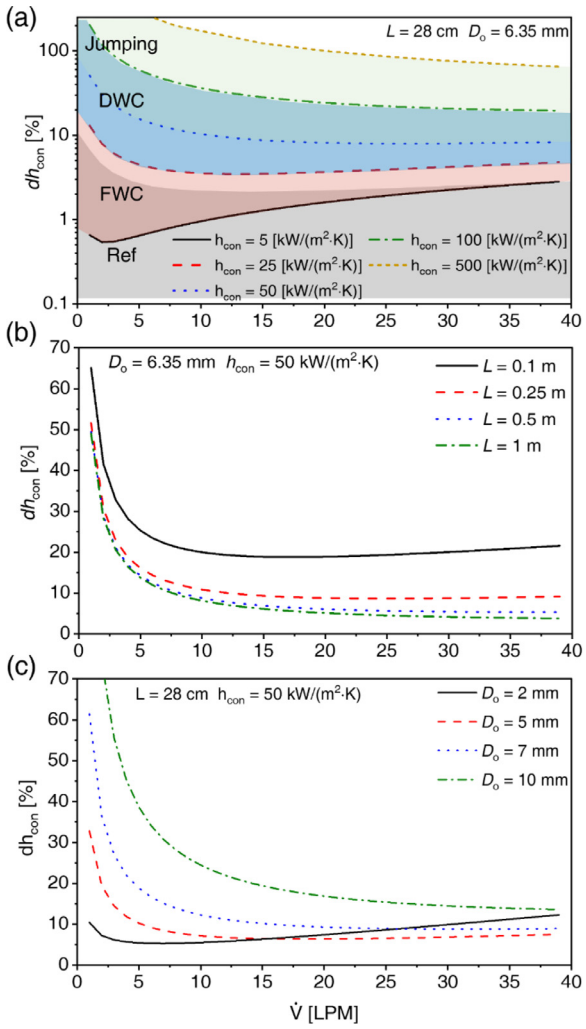

Fig. 3. Uncertainty analysis of the tube condensation heat transfer coefficient (h_{con}). (a) Condensation heat transfer coefficient relative uncertainty (dh_{con}) as a function of volumetric coolant flow rate ($\dot{V}$) for varying h_{con}. Results shown are for fixed $dT = 0.1$ °C, $L = 28$ cm, and $D_o = 6.35$ mm. The shaded regions show four different uncertainty ranges for typical h_{con} for four different conditions: refrigerant condensation (Ref, gray shade), steam filmwise condensation (FWC, red shade), steam dropwise condensation (DWC, blue shade), and steam jumping droplet condensation (Jumping, teal shade). (b) Condensation heat transfer coefficient relative uncertainty dh_{con} as a function of $\dot{V}$ for varying tube length (L). Results shown are for fixed $dT = 0.1$ °C, $D_o = 6.35$ mm, and $h_{con} = 50$ kW/(m^2·K). (c) Condensation heat transfer coefficient relative uncertainty dh_{con} as a function of $\dot{V}$ for varying D_o. Results are for fixed $dT = 0.1$ °C, $L = 28$ cm, and $h_{con} = 50$ kW/(m^2·K). Tube wall thickness is 1.6 mm for all cases. (For interpretation of the references to color in this figure legend, the reader is referred to the web version of this article.)

For extremely small tubes ($D_o = 2$ mm), an optimum is present in Fig. 3(c), whereby increasing the coolant flow rate would increase uncertainty. Looking at Eq. (5), with a fixed volumetric flow rate ($\dot{V}$), h_{in} is directly proportional to Re and inversely proportional to D_i. At fixed $\dot{V}$, Re increases for smaller tube diameter (Eq. 21) resulting in higher h_{in}, although at the expense of larger pressure drop. Thus, the dh_{con} is initially lower for smaller tube diameters. However, with the increase in the flow rate, larger tubes become more preferable due to the increased temperature difference across the tube and higher signal-to-noise ratio.

We note that the Petukhov correlation is most accurate for $10^4 < \mathrm{Re} < 5 \times 10^6$, however, a larger range of Re is considered here (Figs. 2 and 3), only for our theoretical analysis. In the experiments, we ensured that Re lies in the proper range to achieve reliable h_{con} estimation. Furthermore, all results shown in Figs. 2 and 3 were further verified by conducting uncertainty propagation in the engineering equation solver (EES) software.

The uncertainty analysis reveals the difficulties of using the classical coolant enthalpy change method in order to accurately determine the condensation heat flux and heat transfer coefficient:

i) The need to utilize highly turbulent coolant flow (Re > 10,000) in order to enable accurate bulk coolant temperature estimation and to minimize the coolant side thermal resistance.
ii) The need for large tube lengths ($L > 50$ cm) especially for steam dropwise condensation in order to achieve reasonable uncertainty in heat flux measurement (< 20%). Excessive tube lengths are not always possible simply due to manufacturing constraints of DWC promoter coatings. For example, deposition chamber size, coating scale up limitations, chemical availability, and cost.
iii) The inability to obtain reasonable uncertainty (< 10%) due to fundamental limitations associated with the use of an internal heat transfer coefficient correlation having a minimum uncertainty of 6% (Petukhov correlation, Eq. 5).
iv) The need for excessive coolant volumetric flow rate (> 30 LPM) in order to achieve reasonable uncertainties (< 20%) resulting in excessive pressure drop though the tube section.
v) The inability to measure local condensation heat transfer coefficient along the tube axis.
vi) The need to ensure hydrodynamically fully developed flow to reliably utilize the Petukhov correlation (Eq. 5).
vii) The need for highly accurate temperature sensors (e.g., class AA RTDs) to ensure reasonable uncertainty (< 20%).

4. Intelligent vision based heat transfer measurement method

Motivated by the uncertainty analysis conducted in Section 3, we propose a simple, yet powerful visualization-based method for DWC heat transfer characterization. First, we discuss two classical image processing methods implemented for our purpose and discuss their failure modes. Then, we propose our robust learning-based method for falling droplet detection which is further post-processed for high-fidelity shedding droplet frequency and condensation heat flux quantification.

Falling droplets from a condensing tube have been detected using high speed video recording at high frame rates (> 200 fps) [29]. However, droplets look deformed when the capture rate is not high enough (~ 30 fps). Therefore, simple visualization methods fail to detect and count these droplets (Fig. 4). One of the traditional methods to compare two images at the same illumination condition analyses the mean square error (*MSE*) of pixel intensities. Taking this idea into account, all the frames (including the reference frame) are first converted from the RGB (red, green, and blue color) space to the gray space and are compared pixel by pixel from left to right and top to bottom with the reference frame to calculate the *MSE* as shown in Eq. (22):

$$MSE\left(\hat{I}, I\right) = \frac{1}{WH} \sum_{w=1}^{W} \sum_{h=1}^{H} \left[\hat{I}(w,h) - I(w,h)\right]^2, \tag{22}$$

where W and H are the image width and height, respectively, $\hat{I}$ is the reference image and $\hat{I}(w,h)$ refers to the pixel intensity of the reference image at the (w,h) location, and $I(w,h)$ is the pixel intensity of the new image at the (w,h) location. A threshold value could be used to detect substantial changes (falling droplet) in the frames (see Appendix A and Fig. A1). A Gaussian filter having a kernel size of 16 and standard deviation of 2.5 was applied to each frame to smooth out the images and minimize noise [51]. These values were chosen via experimentation. However, the *MSE* depends strongly on the image intensity scaling (e.g., lighting condition), and outliers such as local noise or objects with varying

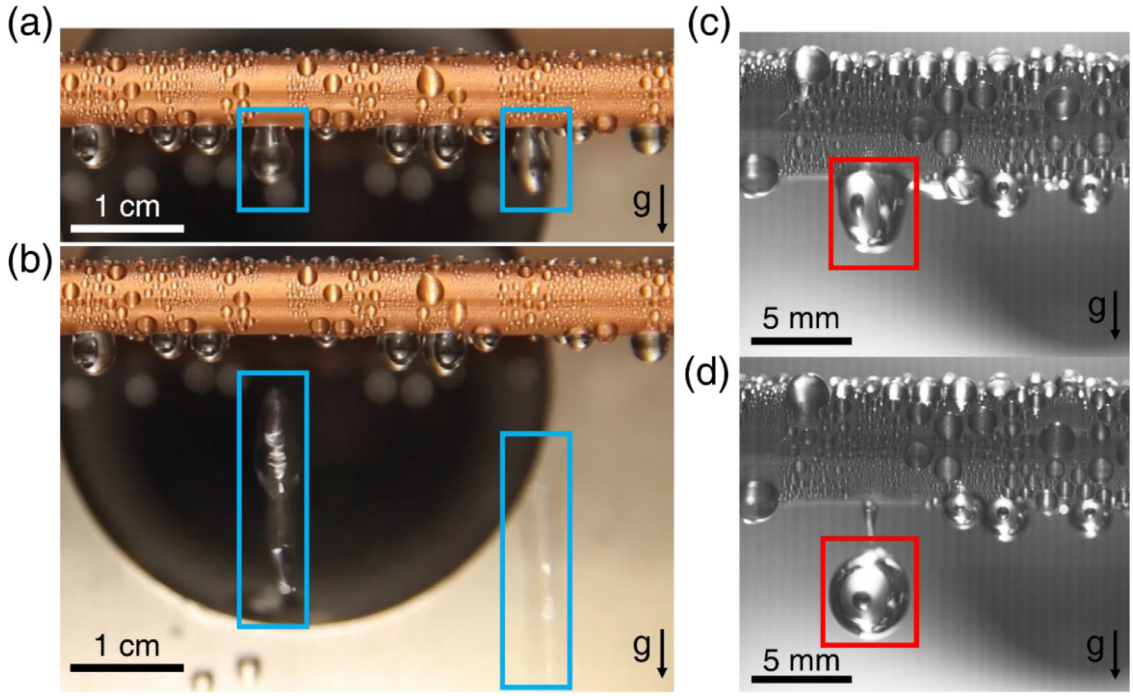

Fig. 4. Optical images of condensate droplets when hanging to the bottom of a copper tube undergoing DWC (a, c) before falling and (b, d) while falling. Video recordings are done at (a, b) 30 fps using a DSLR camera (EOS Rebel T3i, Canon) and (c, d) 300 fps using a high-speed camera (Phantom v7.1, Vision Research). Blue solid outlines identify droplets prior to and after falling in the 30 fps video, while red solid lines identify droplets prior to and after falling in the 300 fps video. The tube sample is made of copper and promoted to ensure DWC of steam via deposition of a Parylene C thin film having thickness of 500 nm ± 100 nm. Experimental conditions: $q'' = 200 \pm 30$ kW/m^2, steam vapor pressure $P = 4 \pm 0.2$ kPa, coolant flow rate $\dot{V} = 15 \pm 0.15$ LPM, $D_o = 6.35$ mm, $D_i = 4.7$ mm coolant inlet temperature $T_{in} = 7 \pm 0.16$ °C. (For interpretation of the references to color in this figure legend, the reader is referred to the web version of this article.)

location in the frames. Furthermore, setting a constant threshold value is not robust enough for many experimental conditions. For example, it is not feasible to find out if more than one droplet is falling.

As another image similarity assessment method, we implemented the structural similarity index metric (*SSIM*) which has gained a lot of attention in the image processing community since its introduction in 2004 [52]. In contrast to *MSE, SSIM* is a similarity metric that varies between -1 and 1, with smaller values indicating lower similarity between the images. *SSIM* compares local patterns of pixel intensities that are luminance and contrast normalized. The *SSIM* is defined as:

$$SSIM(\hat{I}, I) = \frac{(2\lambda_{\hat{I}}\lambda_I + C_1)(2\sigma_{\hat{I}I} + C_2)}{(\lambda_{\hat{I}}^2 + \lambda_I^2 + C_1)(\sigma_{\hat{I}}^2 + \sigma_I^2 + C_2)}, \quad (23)$$

where $\lambda_{\hat{I}}$ and λ_I are the mean intensity of the reference and the new image/patch, $\sigma_{\hat{I}}$ and σ_I are the standard deviation of the reference and the new image/patch, respectively, and C_1 and C_2 are included to avoid instability when $\lambda_{\hat{I}}^2 + \lambda_I^2$ is close to zero [52].

The *SSIM* tends to be a better metric when compared to the *MSE* for falling droplet detection through frame comparison. This is because *SSIM* is more robust to changes in illumination, contrast, and outliers. The *SSIM* tries to find any structural changes within the frames, which is more useful when applied locally rather than globally. Accordingly, we cropped out a window of full length and width of 100 pixels from each frame and calculated the *SSIM* with the reference frame (see Appendix B and Fig. B1). *SSIM* works better when compared to *MSE* when used with a fixed threshold value, especially for cases with low frequency of droplet shedding. Here, values smaller than a specified *SSIM* threshold corresponds to a passing droplet. For high frequency droplet shedding cases (e.g., high condensation heat flux), *SSIM* is more prone to failure.

Two common failure modes exist for *SSIM*. First, it is not feasible to detect simultaneous droplet shedding, which is a common scenario for high condensation heat fluxes. This inability to detect multiple droplets might lead to lower heat flux prediction. Second, in some cases, same droplets in consecutive frames are counted twice and lead to a higher condensation heat flux prediction. Although this error could be minimized by proper choice of window location from which *SSIM* is calculated, complexity of the shedding phenomena (e.g., different droplet velocity and size, droplet coalescence) makes the second error unavoidable. An example of the failure modes is shown in Fig. B1(d) in Appendix B.

Both *MSE* and *SSIM* methods lack reliability to be considered as alternatives to the conventional experimental coolant enthalpy change method (Section 3). Motivated by the recent progress in machine learning (ML) based computer vision techniques for object detection, we developed a framework that takes advantage of the EfficientDet algorithm [53] for falling droplet detection. EfficientDet is a DCNN that uses ImageNet-pretrained EfficientNets [54] as the backbone network and adds a bidirectional feature pyramid network (BiFPN) on top to extract hierarchy of features from input images. Then, it passes the features to the two CNNs responsible for class prediction and bounding box localization. We froze the first two stages of these DCNNs and used them as feature extractors from the condensation videos and retrained the final stage which is responsible for detection and localization of the falling droplets within the frames. Our framework uses the EfficientDet network with three BiFPN layers for hierarchical feature extraction and three convolutional layers in the shared box/class prediction section. It is possible to increase the number of layers for more complex detection and localization problems. However, for our single object detection, three layers were enough to achieve accuracy of more than 97%.

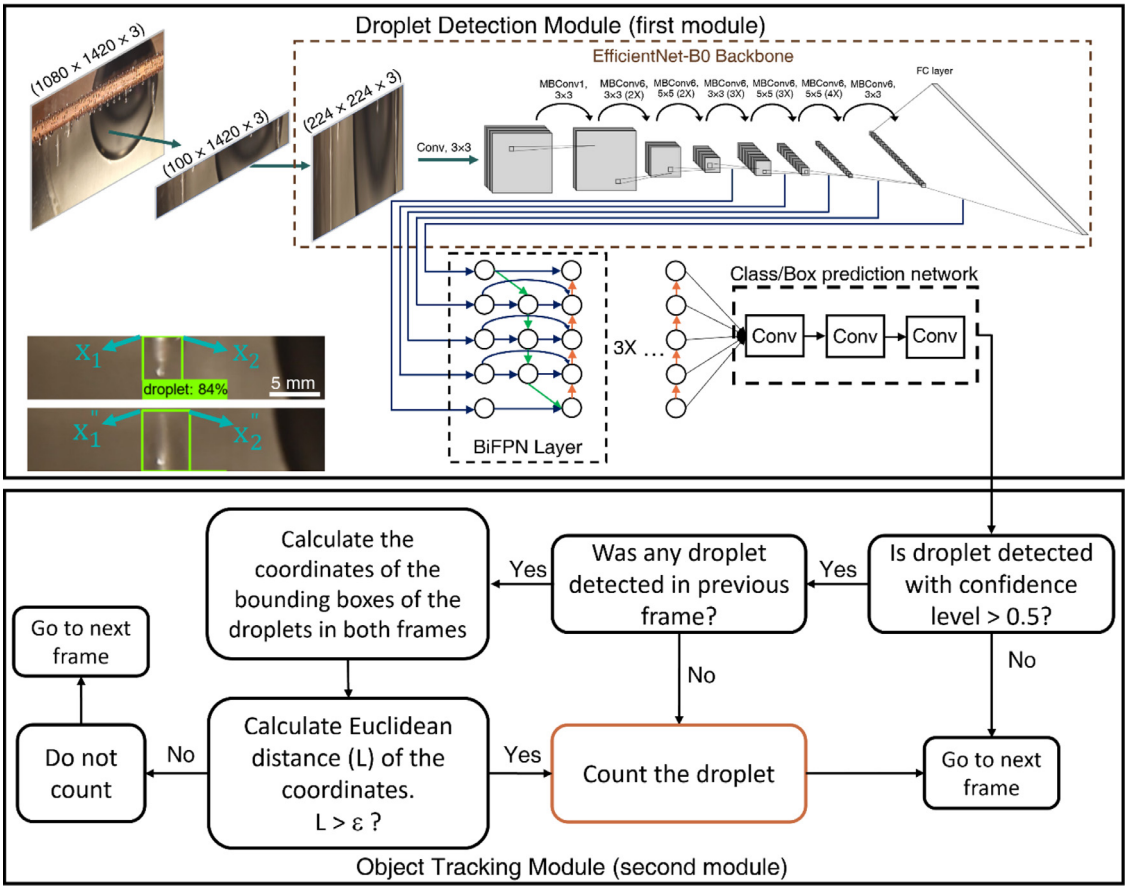

Fig. 5. Machine vision framework for falling droplet detection and robust counting (object tracking) for shedding droplet frequency calculation. Videos of the condensation process were recorded at 30 fps and fed into the droplet detection module frame by frame where each frame is processed through the EfficientDet algorithm which uses the: EfficientNet-B0 as its backbone, 3 layers of BiFPN for scale-invariant feature extraction, and 3 layers of additional convolutional layers as the head for falling droplet detection and localization through bounding boxes. Every detection result is post-processed further for robust shedding frequency estimation.

As shown in Fig. 5, our framework consists of two modules. First module (droplet detection module) is responsible for falling droplet detection where the experimental condensation videos are converted to a tensor containing all frames. Then, a constant area of interest below the condensing tube with size of 100×1420 pixels is cut from each frame with size of 1080×1920 pixels with three channels (RGB color space). The location of the area of interest is chosen with some experimentation. If the area is too close to the tube, hanging droplets may be wrongly detected as falling droplets. Another concern is that a single falling droplet might be counted a few times due to its low initial droplet velocity immediately after tube departure. The second module (object tracking module) in our method is proposed to fully alleviate the later challenge. If the cut area is too far away from the condensing surface, then the velocity of some of the droplets might be too high to be captured by a 30 fps video recording and the 1/30 second interval between the frames would not be enough to capture the droplet. After some experimentation, the area of interest was chosen to be slightly beneath ($\approx$ 8 mm) the condensing tube so that hanging droplets would not appear in these areas. The area of interest is further resized to 224×224 pixels to be compatible with the EfficientNet-B0 input.

Another issue is when a single droplet is counted twice or thrice because the velocity of droplet is not high enough to completely pass the area of interest from one frame to its consecutive frame. Therefore, a single droplet is captured in two or three consecutive frames which results in heat flux overestimation. Our second module (object tracking module) is designed to alleviate this problem. When a droplet is detected, it will check if there were any droplets detected in the previous frame. If detected, it will find the coordinates of the bounding boxes associated with each of the droplets and calculate the Euclidean distance between the coordinates. Here, the Euclidean distance is defined as the length of the segment connecting two points on the plane [55]. If the Euclidean distance is smaller than a pre-set threshold value ($\varepsilon < 4$ pixels), it demonstrates that the two coordinates are close to each other, and same droplet is captured by consecutive frames and therefore only one of the droplets should be counted. If the pre-set threshold is too large, it forces the module not to count droplets that are far and distinct from each other. Conversely, if the pre-set threshold is too small, it loses its ability to detect and reject identical droplets. The threshold should be similar to the localization error of the bounding boxes in the droplet detection module. When the same droplet is detected in two consecutive frames, the coordinates of the bounding boxes around the droplets may slightly vary from each other based on this localization error. Our experiments showed that threshold values between 3 to 6 lead to similar performance.

The convolutional layers and BiFPN layers in EfficientDet are responsible to extract features at different levels of resolution from the input which are passed to the final prediction network for falling droplet detection and localization. Although, convolutional layers alone have been used extensively for feature extraction in object detection networks, recent studies have shown that the different levels of feature hierarchy in convolutional layers could be used to build feature pyramids that will make the network more

Table 2
Advancing contact angle (θ_a), receding contact angle (θ_r), and contact angle hysteresis ($\Delta\theta = \theta_a$ - θ_r) of water droplets on flat Cu samples coated with Parylene C thin films having different thicknesses. Measurements were conducted on five spots on each surface and the average is reported. Standard deviation of the 5 measurements is reported as the uncertainty.

Parylene thickness [μm]	θ_a [deg]	θ_r [deg]	$\Delta\theta$ [deg]
0.5	88.4 ± 3.1	71.2 ± 4.7	17.2 ± 5.7
1	89.4 ± 0.2	73.6 ± 0.4	15.7 ± 0.5
5	86.0 ± 0.6	69.6 ± 2.2	16.4 ± 2.3

robust to detection at different scales which will increase detection performance [56]. Therefore, we could ensure that falling droplets are detected at different scales with extremely high accuracy.

The swish activation function was used after each layer to impose non-linearity to the network [57] and the network was trained end to end with a training dataset of 350 images with fine tuning based on the results achieved on a validation dataset of 220 images. Finally, performance of the network was evaluated on an unseen dataset (test dataset) having 190 images. The dataset contained images of blurry droplets captured from videos at low frame rates (~30 fps). As the network performed well with these blurry images, it showed that even out of focus droplets can be detected with this network. Intersection over union (IoU) [58] of the detected bounding boxes and ground truth boxes was used as the metric for true or false positive criteria. As the purpose of our method is mainly counting the droplets and not identifying the exact localization of each droplet, we relaxed the IoU criteria to 0.5, where detections with IoU value of 0.5 or greater were considered as true positives. At this IoU criteria, the final test precision and recall were 97%.

5. Results and discussion

5.1. Validation of the ML-based method

We conducted two different sets of experiments to evaluate the performance of the developed machine vision framework for real condensation heat transfer measurements. First, we tested three different smooth copper (Cu) tubes having constant external diameter, internal diameter, and length of $D_o = 0.63$ cm, $D_i = 0.47$ cm, and $L = 28$ cm, respectively. Each tube was coated with a hydrophobic promoter through chemical vapor deposition (CVD) of Parylene C in reduced pressure conditions.

Briefly, commercial Cu tube samples (Multipurpose Cu, #8967K88, McMaster-Carr) were purchased and cut to length ($L \approx 28$ cm). Then, cleaning of the internal and external surfaces was completed using sonication in acetone (CAS #179124, Sigma Aldrich), ethanol (CAS #443611, Sigma Aldrich), and DI water (in sequence) for 10 min each. After cleaning, the tubes were placed in a commercial Parylene C deposition chamber (Labcoater 2 Parylene deposition system, Specialty Coating Systems) with an approximate deposition rate of 17 nm/minute. Parylene C was chosen as the promoter of choice mainly due to its ability to achieve conformal depositions, its low surface energy (hydrophobic), and its very reasonable durability during moisture exposure or steam condensation [59,60]. Parylene C is highly durable and possess high chemical stability allowing the surface to keep the same condition over the several steam condensation experiments which assure repeatability of the results [59]. We conducted condensation experiments on each surface at least two independent times to ensure repeatability of the results and data consistency. Microgoniometric water contact angle measurements on flat Parylene C coated Cu tabs are summarized in Table 2 below.

Each individual tube was coated to have a different thickness of Parylene C (500 nm, 1 μm, and 5 μm) and was tested separately in the experimental facility (Fig. 1, Table 1). Condensation heat flux was calculated using both the conventional coolant enthalpy change method (Section 3) and the machine vision method (Section 4). The frequency of droplet shedding from the condensing tube was calculated by dividing the number of droplets detected by the total condensation time of each video (> 5 min at each vapor pressure) using the framework (Fig. 5) proposed in this work. For an accurate frequency estimation, each video was taken for a long time to make sure that at least 1000 droplets are counted. This frequency value was then used to estimate the condensation heat flux using Eq. (24), where $\dot{m}_c$ is the condensate mass flux, ρ is the condensate density, V is the average shedding droplet volume, F is the droplet shedding frequency, and h_{fg} is the latent heat of vapor-to-liquid phase change.

$$q'' = \frac{\dot{m}_c h_{fg}}{A_o} = \frac{\rho V F h_{fg}}{A_o} \,. \tag{24}$$

The heat flux measurement results using both methods including uncertainty bars are shown in Fig. 6. The uncertainty of our developed machine vision method was < 10% and did not vary with the condensation heat flux. The overall uncertainty of the machine vision technique includes uncertainties associated with the droplet shedding frequency, droplet volume calculation, and sample outer surface area. The droplet volume calculation has the highest contribution to the overall uncertainty (> 60%). The uncertainty of the droplet shedding frequency was assumed to be 3% based on the accuracy of the framework shown in Fig. 5. The uncertainty of surface area was calculated based on the measurement accuracies reported in Table 1, and uncertainty of droplet volume was estimated based on the standard deviation over at least 10 droplets at each steam pressure (Fig. C1, Appendix C). We note that temperature sensor and flow meter uncertainties are excluded here as they are not required in this method. The heat flux uncertainty also did not depend on the internal coolant condition and eliminates the uncertainty associated with using the Petukhov correlation for convective heat transfer coefficient estimation (Eq. 5). Therefore, our machine vision method can be used for all internal flow regimes (laminar, transitional, and turbulent) and also for the coolant flow Re ranges where correlations are not accurate enough or are non-existent. Furthermore, developed or developing flow is invariant and not a necessity for the machine vision approach. Finally, the uncertainty for heat flux quantification of our method is not a function of the tube length, diameter, cross-section, or overall shape. Therefore, the proposed machine vision method is highly desirable for conditions where building a large vacuum chamber is a challenge or the tube size is limited by the coating fabrication method.

Fig. 6 shows the results of the heat fluxes measured with experimental enthalpy-based measurement method (Exp) and the visualization-based machine learning (ML) method. Heat fluxes vary with Parylene C layer thickness with the 1 μm thick Parylene C coated Cu tube showing the best performance. The 500 nm layer was not thick enough to fully cover the substrate defects and form a conformal layer. Therefore, droplet pinning was higher on this surface resulting into lower water droplet shedding frequency (Fig. 6a). The results from Table 2 also confirms this as the Cu surface having a 500 nm layer of Parylene C had the highest contact angle hysteresis of the three studied surfaces. For the 5 μm Parylene C coated Cu surface, film uniformity was not an issue. The decreased performance when compared to the 1 μm thick film promoted tube is due to the low thermal conductivity (~ 0.08 W/(m·K)) of the Parylene C material imposing a high conduction thermal resistance which further reduces the heat flux [61]. Thick promoter layers reduce the overall condensation heat trans-

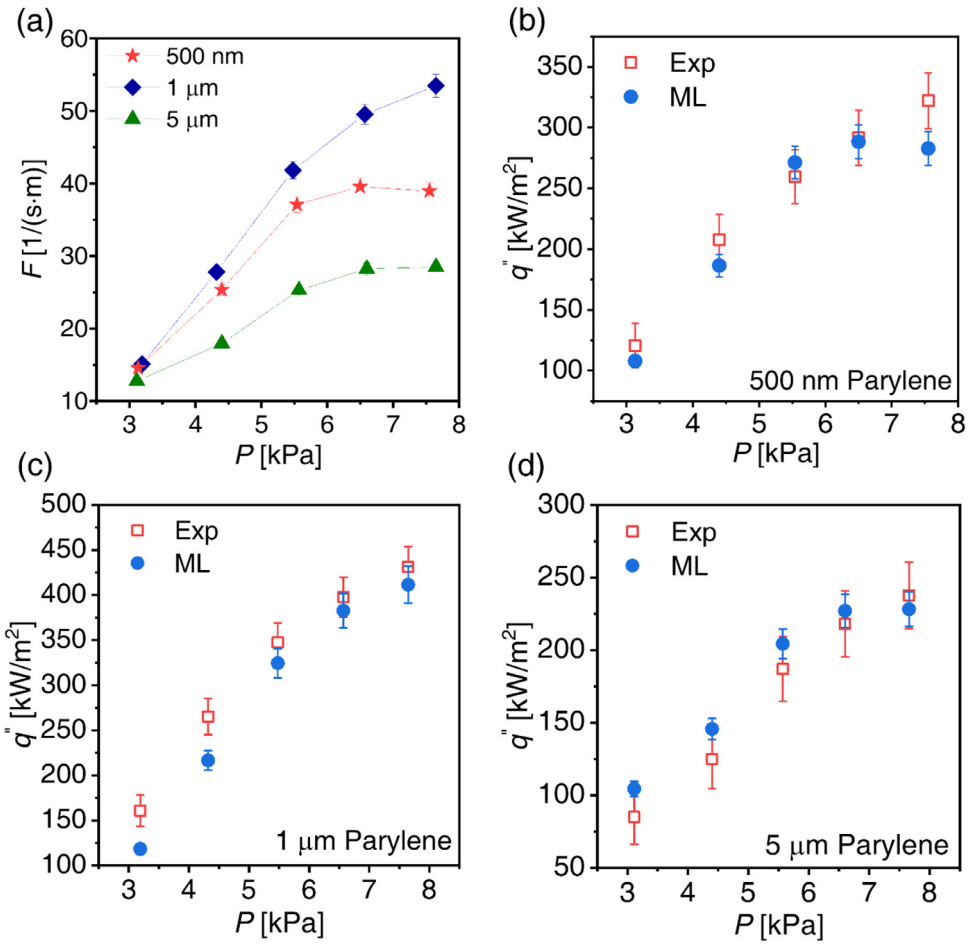

Fig. 6. (a) Water droplet shedding frequency from the hydrophobic Parylene C promoted Cu tubes during DWC of steam obtained using the machine learning framework. Connection lines represent guiding lines to guide the reader. (b-d) Heat flux measurement for the hydrophobic Cu tubes using the coolant enthalpy change method (Exp) and the visualization-based machine learning (ML) method. Experimental conditions: $D_o = 6.35$ mm, $D_i = 4.7$ mm, $L = 28$ cm, $\dot{V} = 15$ LPM, $T_{in} = 7$ °C. The error bars for x axis are smaller than the symbols and are not shown here for better clarity.

fer [62] resulting in the lowest performance for the surfaces studied here (Fig. 6).

As shown in Fig. 2, shorter length tubes result in higher relative errors due to the smaller temperature difference across the tubes. For these cases, final uncertainty values could be as high as 100%. Our method alleviates this challenge by removing the dependence on tube size or geometry. The main contribution to the uncertainty of our machine vision method is in the estimation of the average droplet volume. This challenge can be overcome through the use of a single high speed imaging experiment to visualize falling droplets. The falling droplet diameters for different Parylene C film thicknesses and steam pressures are shown in Fig. C1 in Appendix C. The average departing droplet size depends on the surface energy and coating roughness/chemistry and was observed to remain relatively constant throughout the condensation process for a constant tube diameter (D_o).

The high speed imaging experiment was done with the same setup used for condensation experiments. The chamber was fitted with optical viewports on each side of the chamber (Fig. 1a) and therefore, regular imaging (30 fps) and high speed imaging (300 fps) of the condensing tube were conducted simultaneously. Since the coating chemistry and surface energy of our tubes were similar, falling droplet diameters had negligible variation on tubes having different Parylene C thicknesses and for experiments conducted at different vapor pressures (Fig. C1). Therefore, only a single high speed imaging experimentsuffices to conduct a falling droplet size characterization. However, this one-time high speed imaging experiment needs to be re-conducted if surface properties are varied.

5.2. Local condensation heat transfer measurement on a hybrid tube

Since our machine vision method is not dependent on temperature difference measurement, it can be used for local heat flux measurement on condensing tubes. To demonstrate the capability for local heat flux measurement using our method, we fabricated a separate aluminum (Al) tube having three different wettabilities (hybrid tube) at different axial locations. We estimated the heat flux at each individual wettability section through only one experiment by capturing the condensation on the three different sections in one video. Then, we fabricated three separate Al tubes, each having different wettability level identical to each of the sections on the hybrid tube. We compared the results using the coolant enthalpy change condensation heat transfer measurement method.

To fabricate the hybrid tube, we used crystallographic acid etching of Al with hydrochloric acid (HCl) to form porous microstructures [63]. An Al tube section (general purpose Al tubing, #89965K431, McMaster) having length $L = 9$ cm, outer diameter $D_o = 6.35$ mm, and wall thickness of 1.6 mm was axially divided into three different regions (each one with approximate 3 cm axial length). Prior to surface fabrication, the Al tube was thoroughly cleaned. First, the tube sample was sonicated in acetone for 10 min.

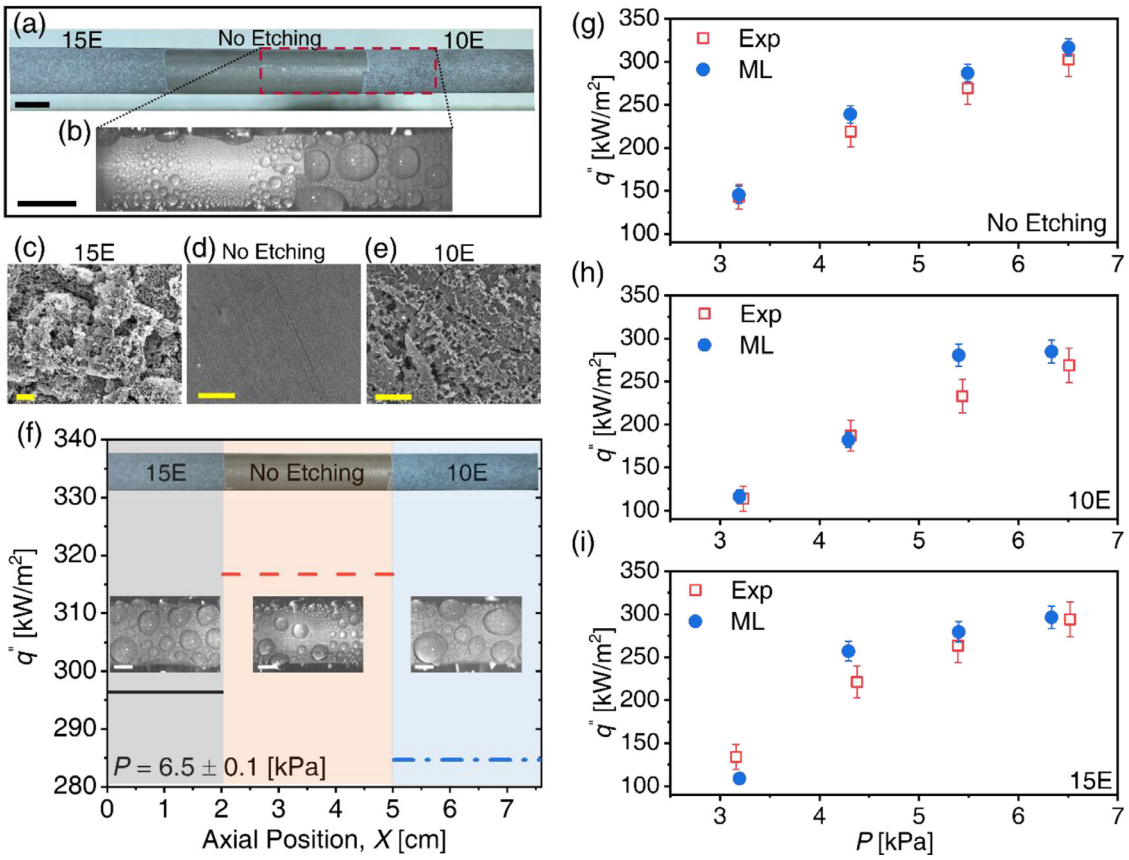

Fig. 7. Local heat flux measurement using the visualization-based machine learning method (ML). The values are compared with the experimental method (Exp) where each tube with a single wettability was tested separately for validation of the local measurements. (a) Photograph of the hybrid tube consisting of three regions defined as 15 min etched (15E), no etching, and 10 min etched (10E). (b) Photograph of the boundary between two of the regions (15E and no etching) during a condensation experiment. (c-e) SEM images of 15 min etched 6061 aluminum, 6061 aluminum, and 10 min etched 6061 aluminum. (f) Heat flux variation along the axial length of the hybrid tube (x-axis) as measured with the ML method in a single experiment. Sub-figures show droplets on each surface during condensation experiment. (g-i) Heat flux measurement results. Here, ML represents local heat flux measurements on a single tube in a single experiment, while Exp represents global measurements from three different experiments on three different tubes. The error bars in the experimental data (Exp) stem from uncertainty analysis (Section 3) while the error bars for the ML method data stem from the uncertainty analysis of Eq. (24). Scale bars in (a and b): 5 mm, scale bars in (c-e): 100 μm, scale bars in sub-figures in (f): 2 mm.

Table 3
Advancing contact angle (θ_a), receding contact angle (θ_r), and contact angle hysteresis ($\Delta\theta = \theta_a$ - θ_r) on plain Al (No Etching), 10 min etched Al (10E), and 15 min etched Al (15E). All samples were conformally coated with a 2 μm Parylene C film. Measurements were conducted on five spots on each surface and the average is reported. Standard deviation of the 5 measurements is reported as the uncertainty.

Surface	θ_a [deg]	θ_r [deg]	$\Delta\theta$ [deg]
No Etching	91.4 ± 0.3	76.3 ± 0.5	15.1 ± 0.6
10E	130.7 ± 4.5	102 ± 4.9	28.7 ± 6.7
15E	121 ± 5.8	97.7 ± 5.7	23.3 ± 8.2

After sonication, the sample was sequentially rinsed with acetone, isopropanol, DI water, and again isopropanol followed by drying with a clean nitrogen gas flow. A 2 M HCl solution was used as the etchant. The first region was etched for 10 min (Fig. 7a, 10E), the middle region was masked with Kapton polyimide plastic tape (# 7648A861, McMaster) and was not etched (Fig. 7a, No Etching), and the last region was etched for 15 min (Fig. 7a, 15E). Selective etching was achieved by partial immersion of the tube in the etchant solution. Then, all the three regions were coated with a 2 µm thick layer of Parylene C to fabricate surfaces with varying levels of hydrophobicity and droplet adhesion (depending on the axial region). Goniometric measurements using water droplet revealed that the apparent advancing and receding contact angles of the surfaces varied (Table 3). The thickness of the Parylene C deposition was rationally chosen in order to fill the roughness cavities while maintaining roughness on the finished surface. A thinner deposition would have promoted superhydrophobicity and droplet jumping, while a thicker deposition would have resulted in similar droplet shedding behavior between the etched and smooth surfaces due to complete filling (and overfill) of the structures. A 2 µm thick Parylene C deposition ensured DWC on all sections with clearly differing droplet departure sizes and distributions (Fig. 7b).

Due to the different roughness at each axial region, droplet adhesion was different depending on where droplets condensed. The unetched (No Etching) region was the smoothest region, followed by the 10 min etched (10E) and 15 min etched (15E) regions, resulting in different condensation performance on each section. These three regions on the same tube were tested during a single condensation experiment using the facility shown in Fig. 1. For comparison, three different tubes with identical wettabilities to each independent region on the hybrid tube were tested separately (3 separate experiments) with results shown in Fig. 7. The local measurements using the ML approach were consistent with the three separate coolant enthalpy-change measurements. This is an important benefit of the ML method as it makes the local heat flux measurement rapid and reliable in a non-intrusive manner.

Given the recent progress in the ML models and methods, more studies in the thermofluidic field will take advantage of ML [64]. One of the drawbacks of these models is the black box approach taken for the development of ML methods that suffer from poor

understanding of what the method is really doing and reporting. However, ML does not need to be a black box approach. ML can be used to learn and identify previously unexplored features from complex physical phenomena that are not yet well-understood. ML can also be used for physical feature extraction that could be post-processed for parameter estimation (similar to this work). Nevertheless, ML models are promising alternatives to conventional methods that lack reliability, have high cost, and are time consuming.

Here we developed a framework consisting of a DCNN for falling droplet detection from 30 fps videos and a post-processing step for robust droplet shedding frequency and heat flux estimation. The uncertainties in the conventional coolant enthalpy-change condensation heat flux measurement methods are typically $>20\%$ with many approaching 100% depending on the temperature sensors used, data acquisition accuracy, coolant flow rate, and tube geometry. Our method achieves lower uncertainty for heat flux estimation ($\sim$10%). More importantly, the uncertainty of the proposed method is not a function of many of the aforementioned experimental parameters. Therefore, it enables reliable condensation heat flux measurement at any flow rate, any tube length and diameter, tube cross sectional geometry, and without any temperature measurement for the coolant or tube surface. The falling droplet detection module (Fig. 5) takes advantage of a state-of-the-art DCNN (EfficientDet) with ImageNet-pretrained EfficientNet-B0 as the backbone coupled to three layers of BiFPN for hierarchical feature extraction which helps to detect droplets at different length scales. This network achieved 97% accuracy over the test dataset consisting of 190 images with varying lighting conditions, tube surfaces (varying surface reflectance), heat fluxes, and droplet shedding frequency. The uncertainty of conventional methods is dependent to heat flux, and it is smaller at higher heat fluxes. Therefore, advantages of our ML method are seen at lower heat fluxes (<500 kW/m^2). However, our ML method possesses similar uncertainty levels at higher heat fluxes while eliminating the requirement for temperature sensors, specified tube geometries, and high coolant flow rates.

Since our ML method only relies on visual data and is not based on temperature difference measurement, it can be used for local condensation heat flux measurement. Therefore, heat fluxes across a tube having homogeneous or different wetting properties (e.g., different coatings) can be measured in a single experiment. This not only saves time by compiling several experiments into one, but also provides opportunity for clearer comparison between different tube designs by ensuring that the experimental condition is identical for all sections on the tube. Although it is possible to ensure consistent experimental conditions by taking precautions from one experiment to another, discrepancies between experiments can arise (e.g., NCGs levels). Hence, comparison within a single test run is always more rigorous when compared to different and independent experimental runs.

The reported method is developed for the dropwise condensation mode where discrete droplets fall down from the bottom of condensing tubes or samples. However, the method can be adapted to handle hybrid dropwise and filmwise condensation that occurs on biphilic surfaces with varying wettability [65–68]. During hybrid condensation, the size of the departing droplets is generally larger when compared to the dropwise condensation mode. The current droplet detection module (Fig. 5) was trained using blurry and deformed droplets having different sizes. However, more images with bigger droplet sizes can be included in the training dataset to ensure that the network learns to detect droplets over a wider range of sizes. Another condensation mode of interest is jumping droplet condensation on superhydrophobic surfaces where droplets can undergo coalescence-induced droplet jumping independent of gravity [69–71]. Our current model is not accurate enough to analyze the jumping droplet condensation mode due to out of plane droplet departure. However, we emphasize that the present ML method can be improved to be more robust by adding readily available features. For example, multi-sectional experiments can be realized by training the ML model to learn additional texture-specific visual features such as jumping droplets from superhydrophobic nanotextured surfaces. Recent studies have demonstrated that ML models are easily adapted to new surfaces, even more so under similar visualization conditions [36,38,72]. Furthermore, our droplet counting module can be extended to accommodate high heat flux (e.g., 100 W/cm^2) cases that are typified by high shedding frequencies. High shedding frequencies pose a challenge for the current droplet counting module because two different droplets that are shed from the same nucleation site could have the same Euclidean distance in consecutive frames as that of a single droplet passing through the specified window. This challenge can be addressed by adding spatial features (e.g., area, orientation, eccentricity) in addition to the Euclidean distance screening algorithm to further distinguish droplets based on higher-level visual similarity.

Finally, while a high-speed camera is still used within this work to measure the shedding droplet diameter, high speed imaging can be fully eliminated in the future by employing image reconstruction techniques [73,74]. For demonstrative purposes, we show that our framework is robust even for low (30 fps) frame rates. Under these conditions, droplets have high distortion (Fig. 4) and are difficult to analyze using conventional methods. However, recent works have demonstrated the successful reconstruction of images with similar motion blur as observed in our experimental data [75]. Since most commercial devices including smartphones support at least 60 fps, we expect accelerated progress in developing deblurring techniques with higher quality image datasets. This will allow reconstruction of high quality images typically obtained from high frame rate imaging ($\sim$ 300 fps) from videos operating at lower frame rates ($\sim$ 60 fps). This can in turn be used for falling droplet size characterization resulting into exclusion of high speed cameras for this required task.

Here, we showed the application of our ML method for DWC. However, our method requires re-training with additional visual data for condensation on superhydrophobic surfaces containing droplets as small as 100 μm for applicability with the jumping droplet condensation mode.

Among the previous works that use ML models for characterizing phase change heat transfer phenomena, the majority of studies are based on using a non-linear regression model such as artificial neural networks (ANN) that are trained on data from experimental measurements [76,77]. Therefore, these data contain measurements uncertainties. Using visual data can alleviate this problem. However, fewer studies have investigated using visual data with ML models for condensation heat transfer characterization.

Future work is needed to modify our developed ML framework to enable direct condensation heat transfer coefficient estimation. One potential approach could use recurrent neural networks (RNNs) [78] that can learn from sequences of data containing droplet nucleation, growth and coalescence on tubes as well as shedding from tubes while taking into account the frequency of the repetition of these stages.

Conclusions

In this study, a visualization-based machine learning framework is developed for high fidelity condensation heat flux characterization. A thorough uncertainty analysis of current condensation experimental methods is provided with effects of different parameter variables such as sample size, coolant mass flow rate, and temperature sensor uncertainty discussed. Motivated by the relatively

high uncertainties of current heat flux measurement approaches, we developed a new framework that takes advantage of deep convolutional neural networks for feature extraction from condensation videos and estimation of droplet shedding frequency which is further processed for robust estimation of the heat flux. For training, validation, and testing of the proposed detection module, we collected our own data using an experimental setup. Here, 350, 220, and 190 images were used for training, validation, and testing, respectively. All condensation experiments were conducted in the absence of non-condensable gases. Several Parylene C promoted hydrophobic Cu tubes were tested and the results from the conventional coolant enthalpy-change method and the ML method are reported and compared. Many sources of uncertainty are eliminated by using our ML framework, with uncertainties being invariant to heat flux, tube length, tube diameter, or coolant flow rate. The droplet detection accuracy of the deep network used in our method is 97% and the overall heat flux uncertainty associated with this method was shown to be $< 10\%$. As our method relies only on visual data, it can be used for local heat transfer measurement across the sample. To demonstrate this added benefit, we conducted a set of experiments on a hybrid tube having three different wettabilities, with heat flux at each region predicted using only one experiment. Our work provides a reliable, and cost-effective method for condensation characterization by removing constraints associated with classical methods such as the requirement for high coolant flow rates, long tube samples, and accurate temperature sensors.

Declaration of Competing Interest

The authors declare no conflict of interest.

CRediT authorship contribution statement

Siavash Khodakarami: Conceptualization, Data curation, Formal analysis, Investigation, Methodology, Software, Validation, Visualization, Writing – original draft, Writing – review & editing. **Kazi Fazle Rabbi:** Methodology, Investigation, Validation, Formal analysis, Writing – review & editing. **Youngjoon Suh:** Investigation, Validation, Writing – review & editing. **Yoonjin Won:** Investigation, Validation, Writing – review & editing. **Nenad Miljkovic:** Conceptualization, Methodology, Funding acquisition, Project administration, Resources, Supervision, Validation, Writing – original draft, Writing – review & editing.

Acknowledgements

S.K., K.F.R., and N.M. gratefully acknowledge funding support from the Office of Naval Research under Grant No. N00014-16-1-2625, the National Science Foundation under Award No. 1554249, and the Air Conditioning and Refrigeration Center. N.M. gratefully acknowledges funding support from the International Institute for Carbon Neutral Energy Research (WPI-I2CNER), sponsored by the Japanese Ministry of Education, Culture, Sports, Science and Technology. Y.S., and Y. W. gratefully acknowledge funding support from the National Science Foundation under Award No. 2045322.

Supplementary materials

Supplementary material associated with this article can be found, in the online version, at doi:10.1016/j.ijheatmasstransfer.2022.123016.

Appendices

Appendix A: MSE results

An example of the *MSE* results is shown in Fig. A1. The first row contains the results when no smoothing is applied to the images (e.g., Gaussian filter). The MSE between the reference frame and the frame with a falling droplet is 0.0914. The MSE values between the reference frame and two other randomly chosen frames are 0.0518 and 0.138. One of these values are bigger and the other one is smaller than the MSE of the falling droplet frame and therefore it is not feasible to use a fixed threshold. The MSE method is sensitive to lighting conditions and outliers, and therefore cannot be used as a universal model.

Appendix B: SSIM results

The SSIM results are shown for two cases demonstrating low and high droplet shedding frequency. The low frequency case is an aluminum tube coated with heptadecafluorodecyltrimethoxy-silane (HTMS, Gelest, CAS No. 83048-65-1) through chemical vapor deposition (CVD) at atmospheric pressure. The high frequency case is an aluminum tube coated with a conformal layer of Parylene C which is deposited via CVD at vacuum condition. The coatings properties and deposition procedure are explained elsewhere [59]. Fig. B1(d) shows an image of the condensing tube inside the experimental chamber (low frequency case) with the specified window below the tube and the *SSIM* results for this tube and also the high frequency case (tube image is not shown here) are shown in Fig. B1(b) and B1(c). Fig. B1(d) shows the two common failure modes for the *SSIM* method.

Appendix C: Falling droplet diameters

Average falling droplet diameters on Cu tubes coated with 500 nm, 1 μm, and 5 μm thick Parylene C films during steam condensation at pressures of 3 kPa and 7 kPa (Fig. C1). As shown, the average droplet diameters are reasonably constant for all tested cases.

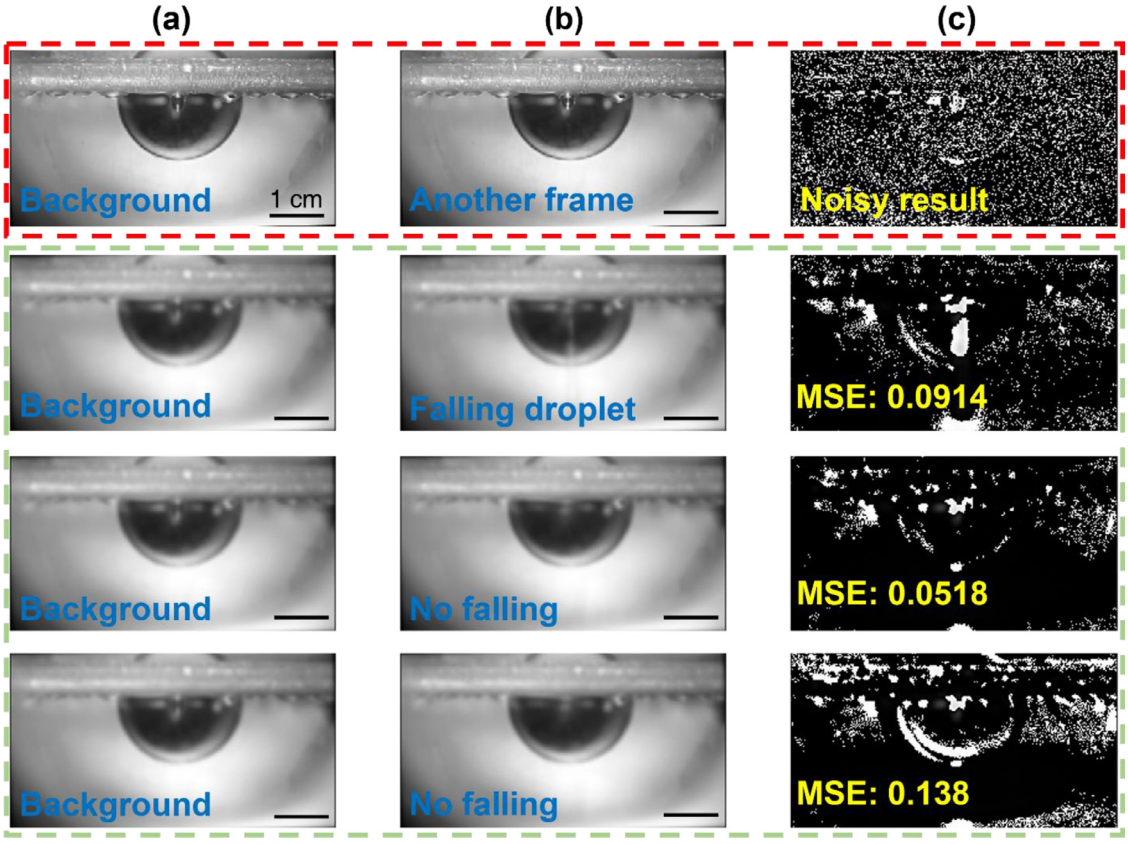

Fig. A1. (a) Background images (reference) used in the *MSE* method. (b) Other frames containing or not containing falling droplets. (c) *MSE* results. First row shows the results before applying the smoothening filter (Gaussian filter). All scale bars are identical for all images and represent 1 cm.

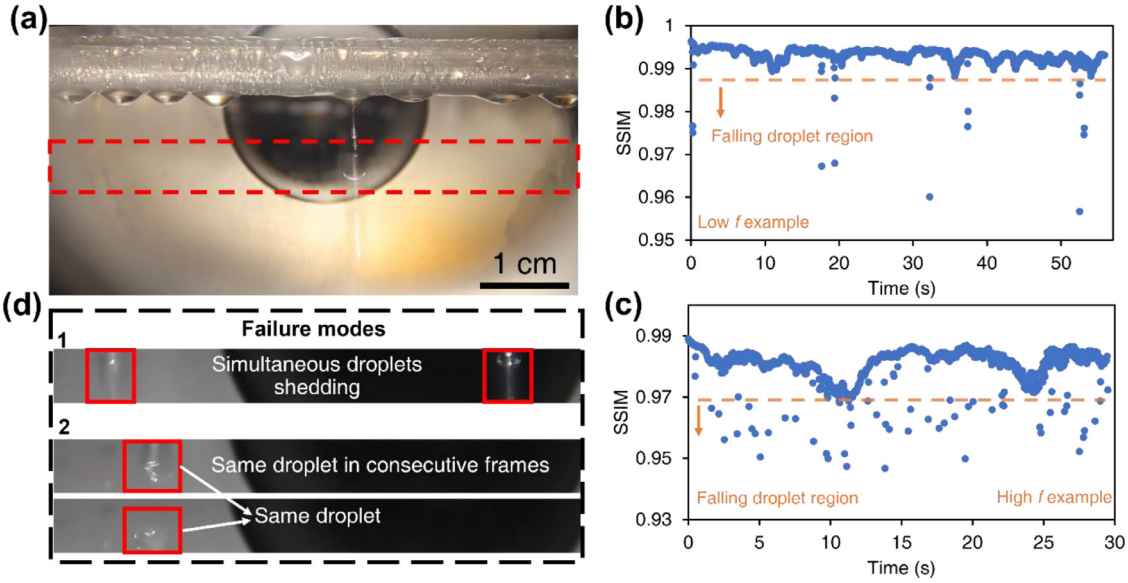

Fig. B1. (a) Photograph of the condensing tube with the specified window (red dashed rectangle box) which is used for *SSIM* calculation. (b) *SSIM* result for a low frequency droplet shedding case. (c) *SSIM* results for a high frequency droplet shedding case. (d) Photographs showing two common failure modes of the SSIM method. (For interpretation of the references to color in this figure legend, the reader is referred to the web version of this article.)

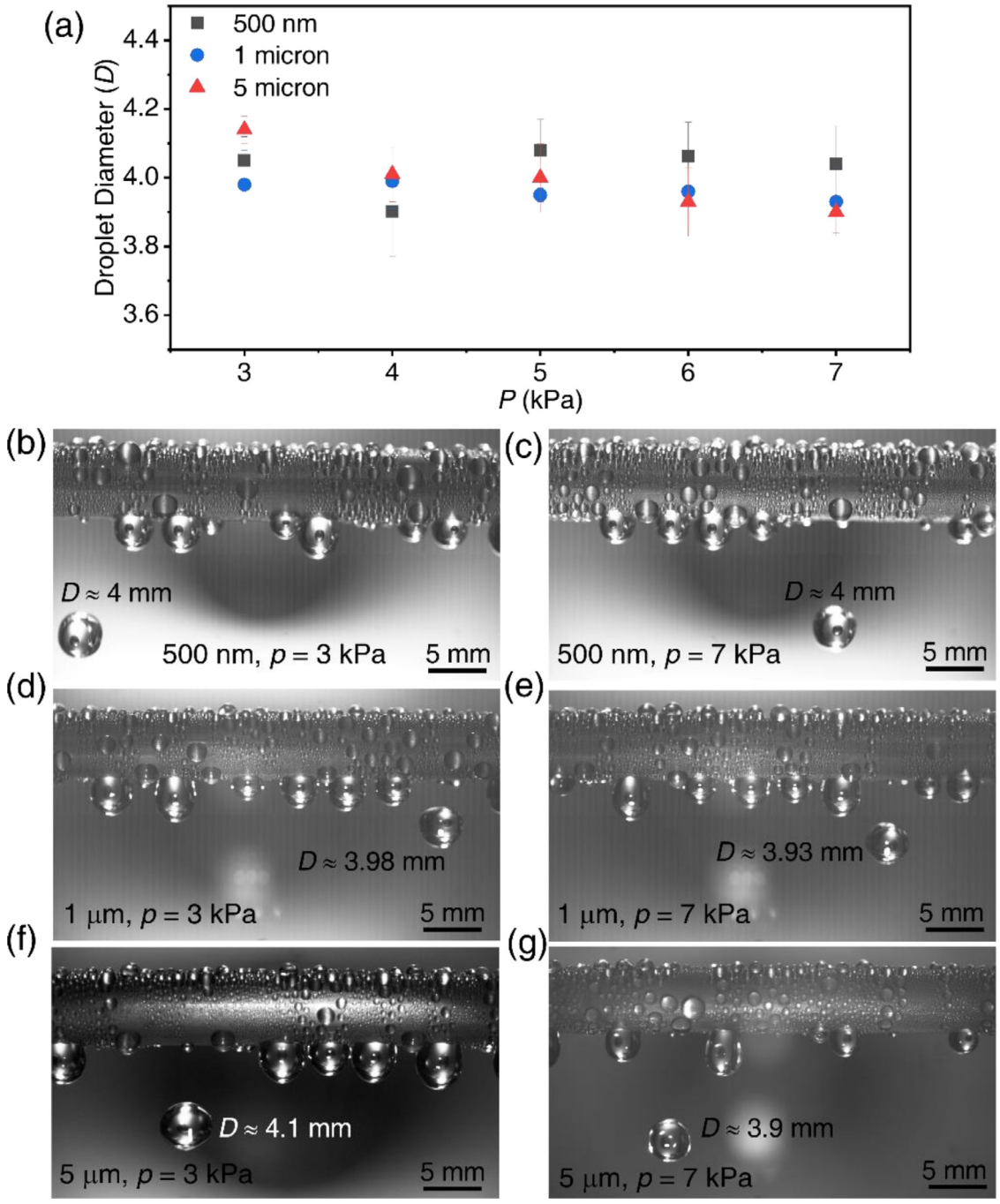

Fig. C1. (a) Average falling droplet diameter during steam SWC at steam pressures ranging from 3 kPa to 7 kPa on Cu tubes promoted with 500 nm, 1 μm, and 5 μm thick Parylene C films. (b- g) Photographs of falling droplets taken from videos recorded at 300 fps for: (b) 500 nm Parylene C thickness and $P = 3$ kPa, (c) 500 nm Parylene C thickness and $P = 7$ kPa, (d) 1 μm Parylene C thickness and $P = 3$ kPa, (e) 1 μm Parylene C thickness and $P = 7$ kPa, (e) 5 μm Parylene C thickness and $P = 3$ kPa, and (g) 5 μm Parylene C thickness and $P = 7$ kPa.

References

[1] K.F. Wiedenheft, H.A. Guo, X. Qu, J.B. Boreyko, F. Liu, K. Zhang, F. Eid, A. Choudhury, Z. Li, C.-H. Chen, Hotspot cooling with jumping-drop vapor chambers, Appl. Phys. Lett. 110 (14) (2017) 141601.
[2] Z. Liu, D.J. Preston, Enhanced Condensation for Improved Energy Efficiency, Joule 3 (5) (2019) 1182–1184.
[3] L. Pérez-Lombard, J. Ortiz, C. Pout, A review on buildings energy consumption information, Energy Build. 40 (3) (2008) 394–398.
[4] H. Cha, H. Vahabi, A. Wu, S. Chavan, M.-K. Kim, S. Sett, S.A. Bosch, W. Wang, A.K. Kota, N. Miljkovic, Dropwise condensation on solid hydrophilic surfaces, Sci. Adv. 6 (2) (2020) eaax0746.
[5] N. Miljkovic, R. Enright, Y. Nam, K. Lopez, N. Dou, J. Sack, E.N. Wang, Jumping–droplet-enhanced condensation on scalable superhydrophobic nanostructured surfaces, Nano Lett. 13 (1) (2013) 179–187.
[6] X.-H. Ma, X.-D. Zhou, Z. Lan, Y.-M. Li, Y. Zhang, Condensation heat transfer enhancement in the presence of non-condensable gas using the interfacial effect of dropwise condensation, Int. J. Heat Mass Transf. 51 (7) (2008) 1728–1737.
[7] J. Huang, J. Zhang, L. Wang, Review of vapor condensation heat and mass transfer in the presence of non-condensable gas, Appl. Therm. Eng. 89 (2015) 469–484.
[8] F.P. Incropera, D.P. DeWitt, T.L. Bergman, A.S. Lavine, Fundamentals of heat and mass transfer, Wiley, New York, 1996.
[9] Z. Song, M. Lu, X. Chen, Investigation of dropwise condensation heat transfer on laser-ablated superhydrophobic/hydrophilic hybrid copper surfaces, ACS Omega 5 (37) (2020) 23588–23595.
[10] X. Ji, D. Zhou, C. Dai, J. Xu, Dropwise condensation heat transfer on superhydrophilic-hydrophobic network hybrid surface, Int. J. Heat Mass Transf. 132 (2019) 52–67.

[11] B. El Fil, G. Kini, S. Garimella, A review of dropwise condensation: theory, modeling, experiments, and applications, Int. J. Heat Mass Transf. 160 (2020) 120172.
[12] T.M. Bandhauer, A. Agarwal, S. Garimella, Measurement and modeling of condensation heat transfer coefficients in circular microchannels, J. Heat Transf. 128 (10) (2006) 1050–1059.
[13] V. Yakhot, S.A. Orszag, A. Yakhot, Heat transfer in turbulent fluids—I. Pipe flow, Int. J. Heat Mass Transf. 30 (1) (1987) 15–22.
[14] J.Z. Fang, D.J. Lee, Micromixing efficiency in static mixer, Chem. Eng. Sci. 56 (12) (2001) 3797–3802.
[15] A. Ghosh, S. Beaini, B.J. Zhang, R. Ganguly, C.M. Megaridis, Enhancing dropwise condensation through bioinspired wettability patterning, Langmuir 30 (43) (2014) 13103–13115.
[16] M.M. Swartz, S.-C. Yao, Experimental study of turbulent natural-convective condensation on a vertical wall with smooth and wavy film interface, Int. J. Heat Mass Transf. 113 (2017) 943–960.
[17] G.-T. Kim, S.-J. Gim, S.-M. Cho, N. Koratkar, I.-K. Oh, Wetting-transparent graphene films for hydrophobic water-harvesting surfaces, Adv. Mater. 26 (30) (2014) 5166–5172.
[18] N. Miljkovic, E.N. Wang, Condensation heat transfer on superhydrophobic surfaces, MRS Bull. 38 (5) (2013) 397–406.
[19] K. Egab, M. Alwazzan, B. Peng, S.K. Oudah, Z. Guo, X. Dai, J. Khan, C. Li, Enhancing filmwise and dropwise condensation using a hybrid wettability contrast mechanism: Circular patterns, Int. J. Heat Mass Transf. 154 (2020) 119640.
[20] B. Peng, X. Ma, Z. Lan, W. Xu, R. Wen, Experimental investigation on steam condensation heat transfer enhancement with vertically patterned hydrophobic–hydrophilic hybrid surfaces, Int. J. Heat Mass Transf. 83 (2015) 27–38.
[21] P.B. Weisensee, Y. Wang, H. Qian, D. Schultz, W.P. King, N. Miljkovic, Condensate droplet size distribution on lubricant-infused surfaces, Int. J. Heat Mass Transf. 109 (2017) 187–199.
[22] S. Lee, K. Cheng, V. Palmre, M.D.M.H. Bhuiya, K.J. Kim, B.J. Zhang, H. Yoon, Heat transfer measurement during dropwise condensation using micro/nano-scale porous surface, Int. J. Heat Mass Transf. 65 (2013) 619–626.
[23] Y. Tang, X. Yang, Y. Li, Y. Lu, D. Zhu, Robust micro-nanostructured superhydrophobic surfaces for long-term dropwise condensation, Nano Lett. (2021).
[24] S. Sett, P. Sokalski, K. Boyina, L. Li, K.F. Rabbi, H. Auby, T. Foulkes, A. Mahvi, G. Barac, L.W. Bolton, N. Miljkovic, Stable dropwise condensation of ethanol and hexane on rationally designed ultrascalable nanostructured lubricant-infused surfaces, Nano Lett. 19 (8) (2019) 5287–5296.
[25] K.L. Wilke, D.S. Antao, S. Cruz, R. Iwata, Y. Zhao, A. Leroy, D.J. Preston, E.N. Wang, Polymer infused porous surfaces for robust, thermally conductive, self-healing coatings for dropwise condensation, ACS Nano 14 (11) (2020) 14878–14886.
[26] R. Wen, Q. Li, J. Wu, G. Wu, W. Wang, Y. Chen, X. Ma, D. Zhao, R. Yang, Hydrophobic copper nanowires for enhancing condensation heat transfer, Nano Energy 33 (2017) 177–183.
[27] K. Rykaczewski, J.H.J. Scott, Methodology for imaging nano-to-microscale water condensation dynamics on complex nanostructures, ACS Nano 5 (7) (2011) 5962–5968.
[28] R.D. Holbrook, K. Rykaczewski, M.E. Staymates, Dynamics of silver nanoparticle release from wound dressings revealed via in situ nanoscale imaging, J. Mater. Sci. Mater. Med. 25 (11) (2014) 2481–2489.
[29] M. Alwazzan, K. Egab, B. Peng, J. Khan, C. li, Condensation on hybrid-patterned copper tubes (II): Visualization study of droplet dynamics, Int. J. Heat Mass Transf. 112 (2017) 950–958.
[30] L. Ma, M. Li, X. Ma, L. Cheng, P. Du, Y. Liu, A review of supervised object-based land-cover image classification, ISPRS J. Photogramm. Remote Sens. 130 (2017) 277–293.
[31] J. Redmon, S. Divvala, R. Girshick, A. Farhadi, You only look once: unified, real-time object detection, in: 2016 IEEE Conference on Computer Vision and Pattern Recognition (CVPR), 2016, pp. 779–788.
[32] K. He, G. Gkioxari, P. Dollár, R. Girshick, Mask r-cnn, in: Proceedings of the IEEE International Conference on Computer Vision, 2017, pp. 2961–2969.
[33] R. Yamashita, M. Nishio, R.K.G. Do, K. Togashi, Convolutional neural networks: an overview and application in radiology, Insights Imag. 9 (4) (2018) 611–629.
[34] N.P. Ramaiah, E.P. Ijjina, C.K. Mohan, Illumination invariant face recognition using convolutional neural networks, in: 2015 IEEE International Conference on Signal Processing, Informatics, Communication and Energy Systems (SPICES), 2015, pp. 1–4.
[35] G.M. Hobold, A.K. da Silva, Visualization-based nucleate boiling heat flux quantification using machine learning, Int. J. Heat Mass Transf. 134 (2019) 511–520.
[36] Y. Suh, R. Bostanabad, Y. Won, Deep learning predicts boiling heat transfer, Sci. Rep. 11 (1) (2021) 5622.
[37] K. Simonyan, A. Zisserman, Very deep convolutional networks for large-scale image recognition, (2014). arXiv preprint arXiv:1409.1556.
[38] Y. Suh, J. Lee, P. Simadiris, X. Yan, S. Sett, L. Li, K.F. Rabbi, N. Miljkovic, Y. Won, A deep learning perspective on dropwise condensation, Adv. Sci. 8 (22) (2021) 2101794.
[39] S. Sett, P. Sokalski, M. Mehta, K.F. Rabbi, A. Gunay, N. Miljkovic, Transient pulse condensation, Appl. Phys. Lett. 117 (9) (2020) 091602.
[40] J.Y. Ho, K.F. Rabbi, S. Sett, T.N. Wong, N. Miljkovic, Dropwise condensation of low surface tension fluids on lubricant-infused surfaces: Droplet size distribution and heat transfer, Int. J. Heat Mass Transf. 172 (2021) 121149.
[41] B.S. Petukhov, An investigation of heat transfer to fluids flowing in pipes under supercritical conditions, International Developments in Heat Transfer: Proceedings of the 1961-62 Heat Transfer Conference, August 28-September 1, 1961, University of Colorado, Boulder, Colorado U.S.A., January 8-12, 1962, Continued discussions, Central Hall Lecture Theatre, Westminster, London, England, (1963).
[42] B.S. Petukhov, Heat transfer and friction in turbulent pipe flow with variable physical properties, in: J.P. Hartnett, T.F. Irvine (Eds.), Advances in Heat Transfer, Elsevier, 1970, pp. 503–564.
[43] https://www.omega.com/en-us/resources/thermocouple-types, in, 2019.
[44] M. Alwazzan, K. Egab, B. Peng, J. Khan, C. Li, Condensation on hybrid-patterned copper tubes (I): Characterization of condensation heat transfer, Int. J. Heat Mass Transf. 112 (2017) 991–1004.
[45] D.J. Preston, D.L. Mafra, N. Miljkovic, J. Kong, E.N. Wang, Scalable graphene coatings for enhanced condensation heat transfer, Nano Lett. 15 (5) (2015) 2902–2909.
[46] A.T. Paxson, J.L. Yagüe, K.K. Gleason, K.K. Varanasi, Stable dropwise condensation for enhancing heat transfer via the initiated chemical vapor deposition (iCVD) of grafted polymer films, Adv. Mater. 26 (3) (2014) 418–423.
[47] A. Bani Kananeh, M.H. Rausch, A.P. Fröba, A. Leipertz, Experimental study of dropwise condensation on plasma-ion implanted stainless steel tubes, Int. J. Heat Mass Transf. 49 (25) (2006) 5018–5026.
[48] K. Navickaitė, L. Cattani, C.R.H. Bahl, K. Engelbrecht, Elliptical double corrugated tubes for enhanced heat transfer, Int. J. Heat Mass Transf. 128 (2019) 363–377.
[49] M.H. Mousa, N. Miljkovic, K. Nawaz, Review of heat transfer enhancement techniques for single phase flows, Renew. Sustain. Energy Rev. 137 (2021) 110566.
[50] T. Alam, M.-H. Kim, A comprehensive review on single phase heat transfer enhancement techniques in heat exchanger applications, Renew. Sustain. Energy Rev. 81 (2018) 813–839.
[51] G. Deng, L. Cahill, An adaptive Gaussian filter for noise reduction and edge detection, in: 1993 IEEE Conference Record Nuclear Science Symposium and Medical Imaging Conference, IEEE, 1993, pp. 1615–1619.
[52] W. Zhou, A.C. Bovik, H.R. Sheikh, E.P. Simoncelli, Image quality assessment: from error visibility to structural similarity, IEEE Trans. Image Process. 13 (4) (2004) 600–612.
[53] M. Tan, R. Pang, Q.V. Le, Efficientdet: Scalable and efficient object detection, in: Proceedings of the IEEE/CVF Conference on Computer Vision and Pattern Recognition, 2020, pp. 10781–10790.
[54] M. Tan, Q. Le, Efficientnet: Rethinking model scaling for convolutional neural networks, in: International Conference on Machine Learning, PMLR, 2019, pp. 6105–6114.
[55] M. D'Agostino, V. Dardanoni, What's so special about Euclidean distance? Soc. Choice Welf. 33 (2) (2009) 211–233.
[56] S. Liu, L. Qi, H. Qin, J. Shi, J. Jia, Path aggregation network for instance segmentation, in: Proceedings of the IEEE Conference On Computer Vision and Pattern Recognition, 2018, pp. 8759–8768.
[57] P. Ramachandran, B. Zoph, Q.V. Le, Searching for activation functions, (2017). arXiv preprint arXiv:1710.05941.
[58] H. Rezatofighi, N. Tsoi, J. Gwak, A. Sadeghian, I. Reid, S. Savarese, Generalized intersection over union: A metric and a loss for bounding box regression, in: Proceedings of the IEEE/CVF Conference on Computer Vision and Pattern Recognition, 2019, pp. 658–666.
[59] S. Khodakarami, H. Zhao, K.F. Rabbi, N. Miljkovic, Scalable corrosion-resistant coatings for thermal applications, ACS Appl. Mater. Interfaces 13 (3) (2021) 4519–4534.
[60] P. Birbarah, T. Gebrael, T. Foulkes, A. Stillwell, A. Moore, R. Pilawa-Podgurski, N. Miljkovic, Water immersion cooling of high power density electronics, Int. J. Heat Mass Transf. 147 (2020) 118918.
[61] T. Takaharu, H. Tanaka, A theoretical study on the constriction resistance in dropwise condensation, Int. J. Heat Mass Transf. 34 (11) (1991) 2779–2786.
[62] J. Rose, Dropwise condensation theory and experiment: a review, Proc. Inst. Mech. Eng. Part A J. Power Energy 216 (2) (2002) 115–128.
[63] N.V. Upot, A. Mahvi, K. Fazle Rabbi, J. Li, A.M. Jacobi, N. Miljkovic, Scalable and resilient etched metallic micro- and nanostructured surfaces for enhanced flow boiling, ACS Appl. Nano Mater. 4 (7) (2021) 6648–6658.
[64] M.T. Hughes, G. Kini, S. Garimella, Status, Challenges, and Potential for Machine Learning in Understanding and Applying Heat Transfer Phenomena, J. Heat Transf. 143 (12) (2021).
[65] J. Xie, Q. She, J. Xu, C. Liang, W. Li, Mixed dropwise-filmwise condensation heat transfer on biphilic surface, Int. J. Heat Mass Transf. 150 (2020) 119273.
[66] J.Y. Ho, K.F. Rabbi, S. Khodakarami, J. Ma, K.S. Boyina, N. Miljkovic, Opportunities in nano-engineered surface designs for enhanced condensation heat and mass transfer, J. Heat Transf. 144 (5) (2022).
[67] M.J. Hoque, X. Yan, H. Keum, L. Li, H. Cha, J.K. Park, S. Kim, N. Miljkovic, High-throughput stamping of hybrid functional surfaces, Langmuir 36 (21) (2020) 5730–5744.
[68] M.J. Hoque, S. Chavan, R. Lundy, L. Li, J. Ma, X. Yan, S. Lei, N. Miljkovic, R. Enright, Biphilic jumping-droplet condensation, Cell Rep. Phys. Sci. 3 (4) (2022) 100823.
[69] J.Y. Ho, K. Fazle Rabbi, S. Khodakarami, X. Yan, L. Li, T.N. Wong, K.C. Leong, N. Miljkovic, Tunable and robust nanostructuring for multifunctional metal additively manufactured interfaces, Nano Lett. 22 (7) (2022) 2650–2659.
[70] J. Koszut, K. Boyina, G. Popovic, J. Carpenter, S. Wang, N. Miljkovic, Superhydrophobic heat exchangers delay frost formation and reduce defrost energy input of aircraft environmental control systems, Int. J. Heat Mass Transf. 189 (2022) 122669.

[71] F. Chu, X. Yan, N. Miljkovic, How superhydrophobic grooves drive single–droplet jumping, Langmuir 38 (14) (2022) 4452–4460.
[72] A. Rokoni, L. Zhang, T. Soori, H. Hu, T. Wu, Y. Sun, Learning new physical descriptors from reduced-order analysis of bubble dynamics in boiling heat transfer, Int. J. Heat Mass Transf. 186 (2022) 122501.
[73] T. Kalluri, D. Pathak, M. Chandraker, D. Tran, Flavr: Flow-agnostic video representations for fast frame interpolation, (2020). arXiv preprint arXiv:2012.08512.
[74] J. Hsieh, E. Liu, B. Nett, J. Tang, J.-B. Thibault, S. Sahney, A new era of image reconstruction: TrueFidelityTM Technical white paper on deep learning image reconstruction, in, 2019.
[75] H. Zhang, Y. Dai, H. Li, P. Koniusz, Deep stacked hierarchical multi-patch network for image deblurring, in: Proceedings of the IEEE/CVF Conference on Computer Vision and Pattern Recognition, 2019, pp. 5978–5986.
[76] L. Zhou, D. Garg, Y. Qiu, S.-M. Kim, I. Mudawar, C.R. Kharangate, Machine learning algorithms to predict flow condensation heat transfer coefficient in mini/micro-channel utilizing universal data, Int. J. Heat Mass Transf. 162 (2020) 120351.
[77] G. Zhu, T. Wen, D. Zhang, Machine learning based approach for the prediction of flow boiling/condensation heat transfer performance in mini channels with serrated fins, Int. J. Heat Mass Transf. 166 (2021) 120783.
[78] W. Zaremba, I. Sutskever, O. Vinyals, Recurrent neural network regularization, (2014). arXiv preprint arXiv:1409.2329.